

## Chapter 5

### Lanthanum Oxide ( $\text{La}_2\text{O}_3$ )

#### 5.1 Introduction

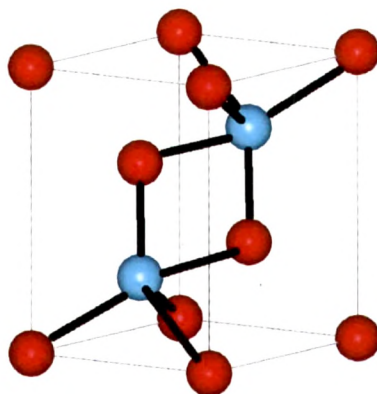
The oxide phosphors with rare-earth photoluminescence in metal oxide matrices have attracted a great deal of attention because of their potential in a host of applications including optoelectronic and flat panel display devices <sup>[1, 2]</sup>. The oxide phosphors possess higher chemical and thermal stability than commonly used sulfide phosphors such as ZnS:Cu, Al and  $\text{Y}_2\text{O}_2\text{S}:\text{Eu}^{3+}$  <sup>[3, 4]</sup>. This advantage makes these materials more chemically stable in high vacuum and under electron excitation. Therefore, there is a continuous search for new oxide phosphors with high performance for phosphor applications. Among others, Lanthanum Oxide,  $\text{La}_2\text{O}_3$ , is interesting because of its versatility and multifunctionality. Lanthanum-based compounds are important particularly in the development of ferroelectric and optical materials.

$\text{La}_2\text{O}_3$  has largest band gap of the rare earth oxides at 4.3 eV, while also having the lowest lattice energy, with very high dielectric constant,  $\epsilon = 27$ . Lanthanum oxide has p-type semi-conducting properties because its resistivity decreases with an increase in temperature, average room temperature resistivity is 10 k $\Omega$ -cm. It is an odorless white solid that is insoluble in water, but soluble in dilute acid. Depending on the pH of the precursor compound, different crystal structures can be obtained. Lanthanum oxide is used to develop ferroelectric materials, such as La-doped  $\text{Bi}_4\text{Ti}_3\text{O}_{12}$  (BLT). Lanthanum oxide is used in optical materials; often the optical glasses are doped with  $\text{La}_2\text{O}_3$  to improve the glass refractive index, chemical durability, and mechanical strength. The addition of the  $\text{La}_2\text{O}_3$  to the glass melt leads to a higher glass transition temperature from 658 °C to 679 °C. The addition also leads to a higher value of density, micro hardness, and refractive index of the glass. Together with oxides of Tungsten, Tantalum, and Thorium,  $\text{La}_2\text{O}_3$  improves the

resistance of the glass to attack by alkali.  $\text{La}_2\text{O}_3$  is an ingredient for the manufacture of piezoelectric and thermoelectric materials. Automobile exhaust-gas converters contain  $\text{La}_2\text{O}_3$ <sup>[5]</sup>. It has been used as a catalyst for the oxychlorination of methane,<sup>[6]</sup> for the destruction of halogenated organic compounds<sup>[6]</sup> and for methane oxidative coupling<sup>[7]</sup>.  $\text{La}_2\text{O}_3$  is also used in X-ray imaging intensifying screens, phosphors as well as dielectric and conductive ceramics.  $\text{La}_2\text{O}_3$  has been examined for the oxidative coupling of methane<sup>[8]</sup>.  $\text{La}_2\text{O}_3$  films can be deposited by many different methods including chemical vapor deposition, thermal oxidation, sputtering and spray pyrolysis. Depositions of these films occur in a temperature range of 250–450 °C. Polycrystalline films are formed at 350 °C<sup>[9]</sup>.

In addition,  $\text{La}_2\text{O}_3$  also has optical applications as a IR-transmitting glass ceramics and as an additive to various transparent ceramic laser materials to improve their optical properties<sup>[10]</sup>. Furthermore,  $\text{La}_2\text{O}_3$ -based glasses have been considered as an ideal material for broadband optical fiber amplifiers<sup>[11]</sup>. Rare earth oxides with large metal to oxygen separation form Hexagonal structures and lanthanum sesquioxide ( $\text{La}_2\text{O}_3$ ) is a typical one in this category. At low temperatures,  $\text{La}_2\text{O}_3$  has an A- $\text{M}_2\text{O}_3$  hexagonal crystal structure. The  $\text{La}^{3+}$  metal atoms are surrounded by a seven coordinate group of  $\text{O}^{2-}$  atoms. The oxygen ions are in an octahedral shape around the metal atom and there is one oxygen ion above one of the octahedral faces<sup>[12]</sup>. Each Lanthanum atom has four Oxygen neighbours at a distance of 2.30 Å and three more at 2.70 Å. The Oxygen atoms have their usual ionic separations with closest O – O distance at 2.75 Å. The metal ion to oxygen ratio [r (R)/r (O)] in this compound is greater than 0.87. At high temperatures the Lanthanum oxide converts to a C -  $\text{M}_2\text{O}_3$  cubic crystal structure. The  $\text{La}^{3+}$  ion in this case is surrounded by a six coordinate group of  $\text{O}^{2-}$  ions<sup>[13]</sup>. Some properties and structural parameters of the oxide are given below.

Formula	Molar mass	Appearance	Density	Melting point	Crystal structure	Space group
$\text{La}_2\text{O}_3$	325.81 g/mol	White hygroscopic	6.51 g/cm <sup>3</sup>	2315°C	Hexagonal (fluorite)	P-3m1

Structure of  $\text{La}_2\text{O}_3$ 

Trivalent Lanthanum has atomic number 57. Like Yttrium( $\text{Y}^{3+}$ ) and Lutetium( $\text{Lu}^{3+}$ ), there are no 4f electrons present and therefore there are no electronic energy levels that can induce excitation and luminescence processes in or near the visible region. Therefore it does not act as an activator. They are transparent for visual light, have no low energy levels and interaction between the rare earth emitting activator ions and the matrix is minimal in these oxides. Hence, it can be a promising host material because of the light absorption through charge transfer band. The energy from charge transfer band is then transferred to doped rare earth ions giving characteristic emissions. Lot of work has been done on  $\text{Y}_2\text{O}_3$  e.g. Lanthanide- doped cubic-phase  $\text{Y}_2\text{O}_3$  and related materials, which are common phosphors in optical display and lighting applications<sup>[14]</sup>. Some work has been done in  $\text{Lu}_2\text{O}_3$  but it still needs to be explored further. Cerium and Terbium co – doped phosphate of Lanthanum is a commercially available efficient green phosphor for Lamp industry<sup>[15]</sup>. Rare earth doped Vanadate of Lanthanum is also used for up conversion processes<sup>[16]</sup>.

Bulk rare earth oxide of Yttrium is an ideal host for photoluminescence and is a commercially available fluorescent powders. Less work is done to investigate  $\text{La}_2\text{O}_3$  as a host for rare earth ions to give luminescent properties.  $\text{Pr}^{3+}$ ,  $\text{Er}^{3+}$  and  $\text{Eu}^{3+}$  activated  $\text{La}_2\text{O}_3$

phosphors have been investigated but not extensively<sup>[17, 18]</sup>.  $\text{Eu}^{3+}$  doped Lanthanum oxide nanoparticles are also being used in down conversion processes in solar systems<sup>[19]</sup>. The radiative transition rate and quantum efficiency of  ${}^5\text{D}_1 \rightarrow {}^7\text{F}_1$  transition in nano wires increased greatly in comparison with nano particles and the corresponding bulk ones<sup>[20, 21]</sup>. This implies that 1-D nano wires doped with rare earth may be ideal nanosized phosphors. The charge transfer energy of Lanthanum Oxide is at lower energy than aluminates, silicates, borates and phosphates<sup>[22]</sup> because the complexes that strongly bind the oxygen 2p electrons are absent in the sesquioxides. Therefore it can be excited at lower energy to give emissions.

The samples of Lanthanum oxide doped with rare earth activators like Europium and Terbium were synthesized by the following methods.

1. Ceramic method (Solid State synthesis )
2. Solution Combustion method
  - I. Furnace Combustion
  - II. Microwave induced combustion
3. Co-Precipitation Method

## 5.2 Synthesis of Samples

Lanthanum Nitrate Hydrate ( $\text{La}(\text{NO}_3)_3 \cdot x\text{H}_2\text{O}$  - 99.99% purity) of China make, Europium Nitrate Hexa hydrate ( $\text{Eu}(\text{NO}_3)_3 \cdot 6\text{H}_2\text{O}$ , 99.9% purity) & Terbium Nitrate Hydrate ( $\text{Tb}(\text{NO}_3)_3 \cdot x\text{H}_2\text{O}$ , 99.9% purity) of Alfa Aesar and Urea ( $\text{NH}_2\text{CONH}_2$ , 99% purity) of Qualigens, were used as the precursor materials.

For the synthesis of Lanthanum oxide by Solid State reaction method, 5 grams of Lanthanum Nitrate was mixed with Europium/Terbium as nitrates in stoichiometric proportion for a 2 mole percent incorporation. A minimum amount of water was added and the contents were mixed thoroughly in agate mortar and pestle. The resulting paste

was transferred into silica crucible and heated at 1100°C for 4 hours. The obtained product was a dense cake which was crushed and grinded to fine powder with mortar and pestle. The powder was washed with acetone to remove the residual impurities like nitrate ions. The final product obtained was white coloured powder.

For synthesis by Furnace combustion method, 5 grams of Lanthanum Nitrate (*oxidizer*) and 2 mole percent equivalent of Europium/Terbium as nitrates was mixed with varying amounts of Urea (*fuel*) for stoichiometric (2.5), fuel rich (3.0) and fuel deficient ratios (2.0) in a 250 ml Schott Duran (Germany) Round Bottom flask. The corresponding equivalence ratio  $\phi_e$  (discussed in Chapter 3) was calculated and found to be 1.0 for stoichiometric, 0.88 for fuel rich and 1.16 for fuel lean ratios. The amount of water added to the mixture was about 0.667 ml/gm of nitrate [ni]. It was heated at moderate rate with stirring for 30 minutes to allow homogenous mixing of the constituents. The mixture was then introduced into a muffle furnace preheated at around 500°C. Initially the mixture starts boiling and slowly the water gets evaporated. The solution (paste) melts (boils) and undergoes dehydration followed by decomposition with the evolution of large amounts of gases (oxides of nitrogen and ammonia). The redox mixture is then auto ignited resulting in an exothermic reaction with an orangish red flame reaching temperature above 1100°C. White fluffy cake was obtained which was voluminous, porous and foamy in nature. This cake was grinded with mortar and pestle to obtain fine powder which was then washed with acetone to remove the residual impurities. The final product was pure white coloured fine powder.

In case of Microwave combustion synthesis, the above mentioned mixtures were taken in a 250 ml Schott Duran (Germany) round bottom flask and placed inside a modified kitchen microwave oven (discussed in chapter 3) with output power of 850 watts and frequency of 2.45 GHz for a few minutes. During this time, the redox mixture boiled with the evolution of large amount of gas, underwent dehydration and ignited (due to internal heating) resulting in an exothermic reaction with a red flame releasing large amount of heat. Here

also, a white cake was obtained which was voluminous, porous and foamy in nature. The powder was washed with acetone to remove the residual impurities and grinded with mortar and pestle. The final product was pure white coloured fine powder.

In Co-precipitation method, 3.249 gram of  $\text{La}(\text{NO}_3)_3$  was dissolved in 50 ml of alcohol to obtain 0.2 mol/liter solution. This solution was added drop wise into an alcoholic solution of 2 mol/liter ammonium hydroxide at the rate of 4 ml/minute and vigorously stirred. The temperature was maintained at  $50^\circ\text{C}$ . As the precipitation occurred, the final pH of the solution was greater than 9. These precipitates were filtered and washed with acetone several times to get rid of residual impurities. The precipitates were dried in a vacuum desiccator for 10-12 hours and finally dried in an oven at  $100^\circ\text{C}$  for 12 hrs. Lanthanum Hydroxide nanoparticles were obtained. These nanoparticles were calcined at  $600^\circ\text{C}$  for 2 hours to obtain the Lanthanum Oxide nanoparticles. The powders thus obtained were collected in glass bottles.

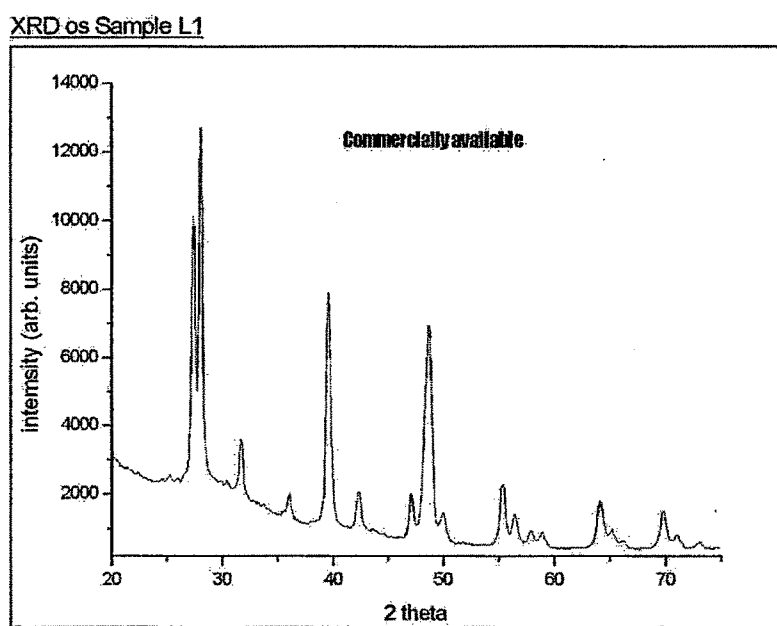
### 5.3 Characterization of Samples

These samples were characterized by X-ray diffraction (XRD). They were further investigated by Scanning electron microscopy (SEM). Their Fluorescence and UV-Visible characteristics were also studied.

#### X - Ray Diffraction

The XRD patterns were taken of Bruker D8 advance X-ray diffractometer. The  $2\theta$  range was taken from  $20^\circ$  to  $75^\circ$  in scan mode with step increment of  $0.050^\circ$  and step time 2 seconds at room temperature. The data were smoothed and then considered. The X ray diffraction patterns of the samples are given below. Out of the total nine samples, three samples have been synthesized by furnace combustion method and other three by microwave combustion method with fuel lean, stoichiometric and fuel rich ratios respectively. One sample has been synthesized by Solid state synthesis method and another by Co –precipitation method. The XRD patterns are given in Figures L<sub>x</sub> 1 to L<sub>x</sub> 9 accordingly. The XRD of commercially available sample is also given for reference.

Lanthanum oxide has been reportedly found to be having a multiplicity of structures. Hence, there are multiple JCPDS files to refer for ascertaining the structure of the synthesized samples. To identify the sample structure, 10 prominent peaks were considered. d values of the peaks were matched with six JCPDS files for hexagonal structure, three JCPDS files for cubic structure and 1 JCPDS file for monoclinic structure. To match the peaks of this sample with the closest structure, correlation function was used. The relevant references have been mentioned for the respective samples.

Figure L<sub>x</sub> 1

XRD of Sample L 2

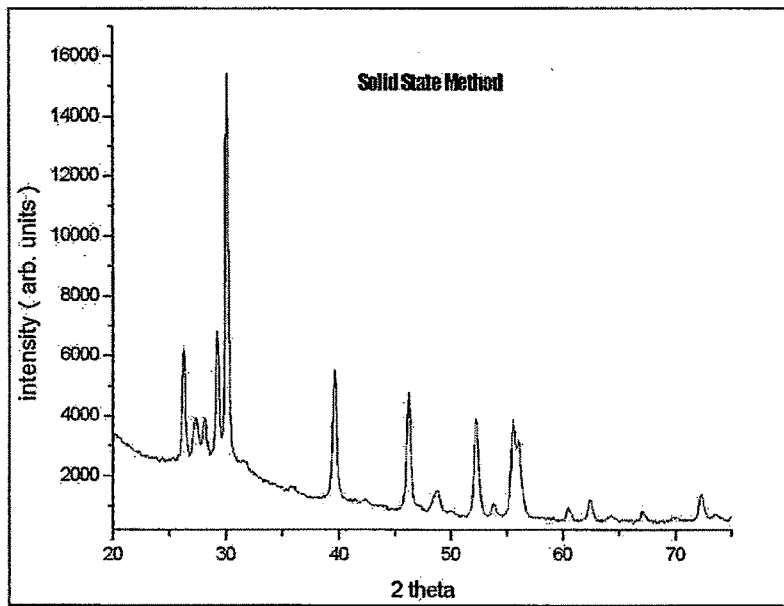


Figure Lx 2

XRD of Sample L 3

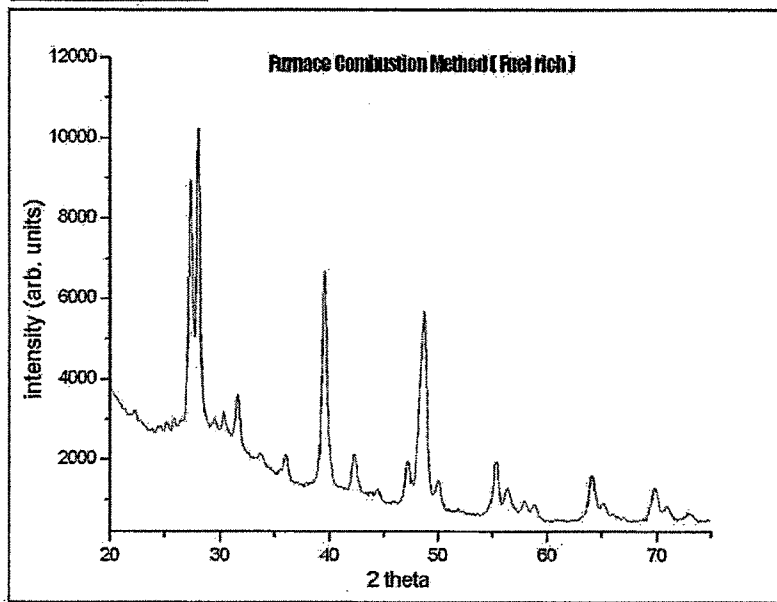


Figure Lx 3

XRD of Sample L 4

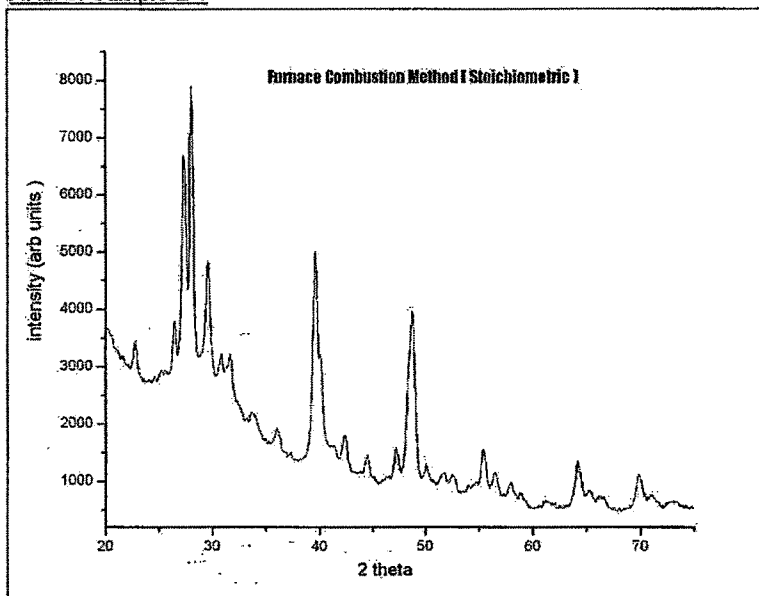


Figure Lx 4

XRD of Sample L 5

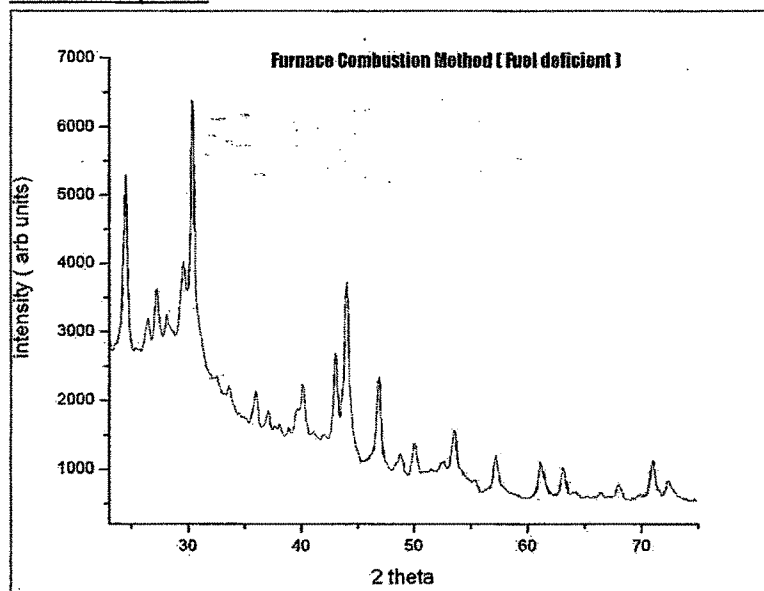


Figure Lx 5

XRD of Sample L 6

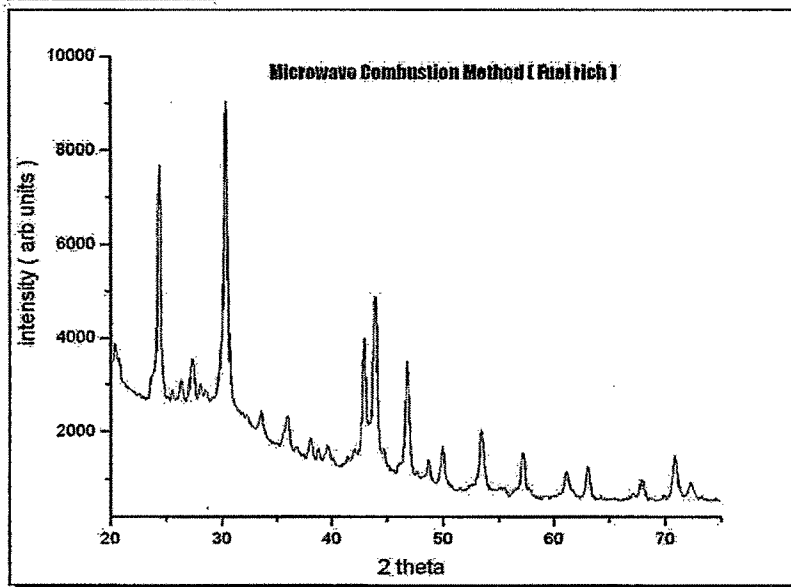


Figure L<sub>x</sub> 6

XRD of Sample L 7

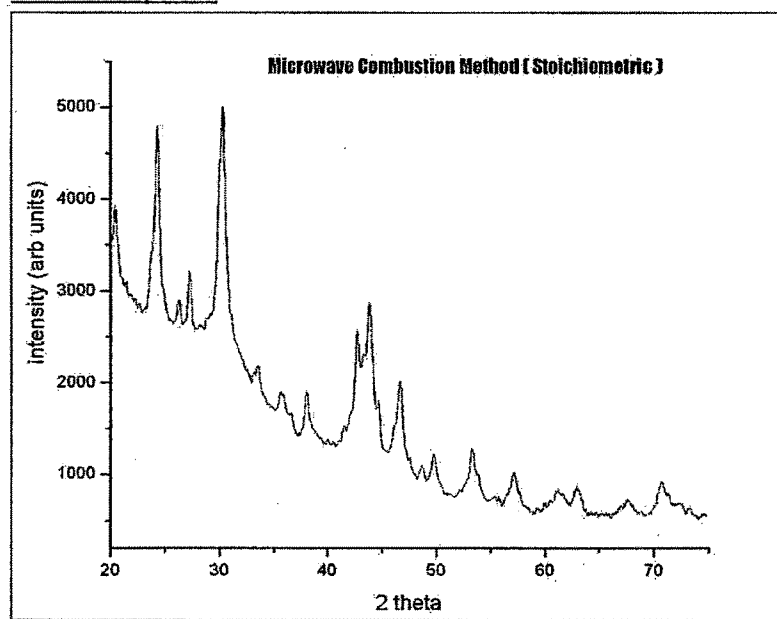


Figure L<sub>x</sub> 7

XRD of Sample L 8

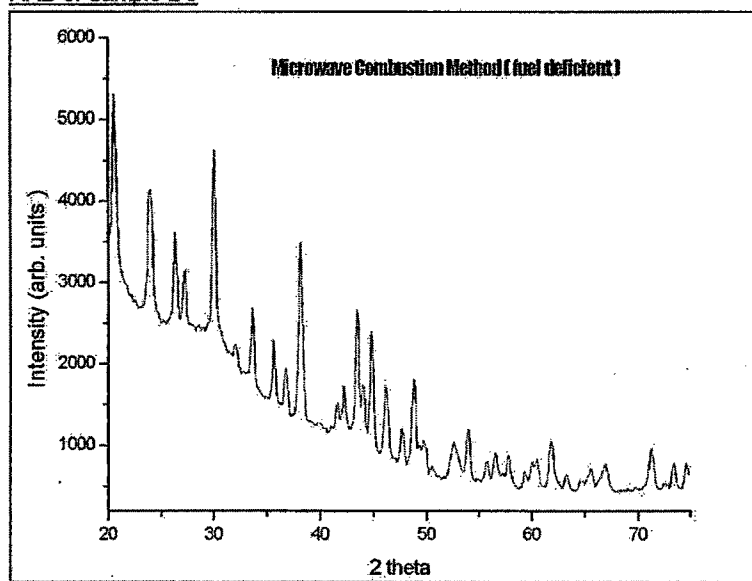


Figure Lx 8

XRD of Sample L 9

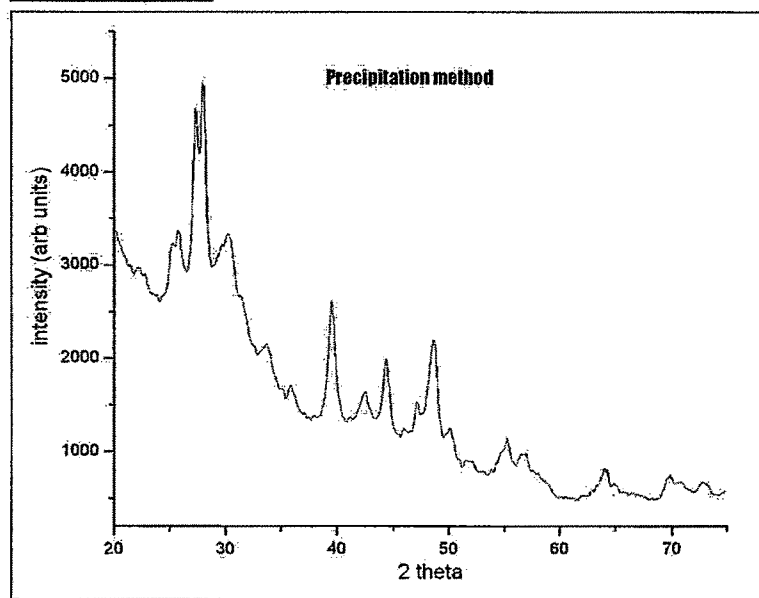


Figure Lx 9

Reflections for sample L1 i.e. commercially available sample show sharp features with high intensity. The split peaks at  $2\theta$  value of  $28.028^\circ$  have the highest intensity followed by peaks at  $27.341^\circ$  and  $39.541^\circ$ . The peaks match most closely to JCPDS file number 83-1355 for hexagonal structure as the value of the co-relation factor in this case was found to be 0.984674. Additionally, there are six peaks of this sample which match closely with the peaks of monoclinic structure in JCPDS file no 22-0641. Four peaks match closely with cubic structure in JCPDS file number 22-0369 and two peaks in JCPDS file number 04-0856. The lattice constant for the (101) and (002) planes is calculated to be 0.42082 nm and 0.65187 nm respectively.

Reflections for sample L2, prepared by solid state method also show sharp features with high intensity. Many peaks are observed. To identify the sample structure, ten prominent peaks were considered. The split peaks at  $2\theta$  value of  $30.057^\circ$  have the highest intensity followed by peaks at  $29.200^\circ$  and  $26.202^\circ$ . The peaks match most closely to JCPDS file number 83-1355 for hexagonal structure, for which the value of co-relation factor was found to be 0.93957. Besides, there are four peaks of monoclinic structure in JCPDS file no 22-0641, five peaks of cubic structure in JCPDS file number 22-0369 and two peaks in JCPDS file number 04-0856 matching closely with the peaks of this sample. The intensities of the peaks are higher than the peaks of sample L1. However the intensity and  $2\theta$  values of some of the peaks of sample L2 are different than L1. Some amount of broadening is observed in the peaks. The lattice constant for (101) and (002) planes is calculated to be 0.42889 nm and 0.67967nm respectively.

Reflections for sample L3, synthesized by furnace combustion method with fuel rich ratio show similar pattern. The split peaks at  $2\theta$  value of  $28.017^\circ$  have the highest intensity followed by peaks at  $27.315^\circ$  and  $39.527^\circ$ . The peaks match most closely to JCPDS file number 83-1355 for hexagonal structure. The value of co-relation factor is found to be 0.920413. There are seven peaks of monoclinic structure in JCPDS file no 22-0641, four peaks of cubic structure in JCPDS file number 22-0369 and two peaks in JCPDS file number 04-0856 matching closely with the peaks of this sample. The intensities of the peaks are

lower than the peaks of samples L1 and L2. The broadening in the peaks is higher than for peaks of sample L2. The lattice constant for (101) and (002) planes is calculated to be 0.42090 nm and 0.65247 nm respectively.

Reflections for sample L4, synthesized by furnace combustion method with stoichiometric ratio show split peaks at  $2\theta$  value of  $28.062^\circ$  having the highest intensity followed by peaks at  $27.348^\circ$  and  $48.734^\circ$ . A co-relation factor of 0.924923 was obtained for JCPDS file number 74-2430 having hexagonal structure. The peaks of this sample match closely with eight peaks of monoclinic structure in JCPDS file no 22-0641, six peaks of cubic structure in JCPDS file number 22-0369 and two peaks in JCPDS file number 04-0856. The intensity of the peaks are lower than the peaks of samples L1, L2 and L3. The broadening in the peaks is less than for peaks of sample L3. There are some more peaks observed in this sample compared to samples L1, L2, L3. The lattice constant for (101) and (002) planes is calculated to be 0.42018 nm and 0.65169nm.

Reflections for sample L5, synthesized by furnace combustion method with fuel lean ratio are given in figure L<sub>x</sub> 5. The peak at  $2\theta$  value of  $30.381^\circ$  has the highest intensity followed by  $24.463^\circ$  and  $29.568^\circ$ . The peaks match most closely to JCPDS file number 83-1355 for hexagonal structure. The co-relation factor is 0.923861. Seven peaks of monoclinic structure in JCPDS file no 22-0641, four peaks of cubic structure in JCPDS file number 22-0369 and two peaks in JCPDS file number 04-0856 also match closely with the peaks of this sample. The intensities of the peaks are lower than the peaks of samples L1, L2, L3 and L4. The broadening in the peaks is higher than for peaks of samples L3 and L4. There are some more peaks observed in this sample compared to samples L1, L2, L3. The lattice constant for (101) and (002) planes is calculated to be 0.37179 nm and 0.72989 nm.

Reflections for sample L6, synthesized by microwave combustion method with fuel rich ratio show sharp features with moderate intensity. The peak at  $2\theta$  value of  $30.316^\circ$  has the highest intensity followed by peaks at  $24.370^\circ$  and  $20.400^\circ$ . The peaks match most closely to JCPDS file number 73-2141 for hexagonal structure. The value of correlation factor is

0.970523. There are five peaks of monoclinic structure in JCPDS file no 22-0641, two peaks of cubic structure in JCPDS file number 22-0369 and three peaks in JCPDS file number 04-0856 matching closely with the peaks of this sample. The intensities of the peaks are lower than the peaks of samples L1, L2, L3 but higher than those for samples L4 and L5. The broadening in the peaks is lower than that for peaks of samples L3, L4 and L5. The lattice constant for (101) and (002) planes is calculated to be 0.37179 nm and 0.72989 nm.

Reflections for sample L7, synthesized by microwave combustion method with stoichiometric ratio also show sharp features with moderate intensity. The peak at  $2\theta$  value of  $30.237^\circ$  has the highest intensity followed by peaks at  $24.284^\circ$  and  $20.404^\circ$ . The peaks match most closely to JCPDS file number 74-2430 for hexagonal structure. The value of the co-relation factor is 0.96705. Six peaks of monoclinic structure in JCPDS file no 22-0641, two peaks of cubic structure in JCPDS file number 22-0369 and another two peaks in JCPDS file number 04-0856 match closely with the peaks of this sample. The intensities of the peaks are lower than for previous samples. The broadening in the peaks is higher than for peaks of samples L1, L2, L3, L4, L5 and L6. The lattice constant for (101) and (002) planes is calculated to be 0.37267nm and 0.73245 nm.

Reflections for sample L8, synthesized by microwave combustion method with fuel lean ratio show sharp features with moderate intensity. The peak at  $2\theta$  value of  $20.507^\circ$  has the highest intensity followed by peaks at  $23.888^\circ$  and  $26.311^\circ$ . The peaks match most closely to JCPDS file number 74-2430 for hexagonal structure with a co-relation factor of 0.978488. There are nine peaks of monoclinic structure in JCPDS file no 22-0641, four peaks of cubic structure in JCPDS file number 22-0369 and two peaks in JCPDS file number 04-0856 match closely with the peaks of this sample. The intensities of the peaks are lower than those for previous samples. The broadening in the peaks is higher than for peaks of samples L1, L2, L3, L4, L5, and L6 but lower than that for sample L7. The lattice constant for (101) and (002) planes is calculated to be 0.37465 nm and 0.74442 nm.

Reflections for sample L9, synthesized by co-precipitation method show sharp features with moderate intensity but a lower degree of crystallinity. The peak at  $2\theta$  value of  $27.947^\circ$  has the highest intensity followed by  $27.253^\circ$  and  $25.751^\circ$ . The peaks match most closely to JCPDS file number 83-1355 for hexagonal structure. The value of co-relation factor is found to be 0.958348. There are six peaks of monoclinic structure in JCPDS file no 22-0641, four peaks of cubic structure in JCPDS file number 22-0369 and one peak in JCPDS file number 04-0856 match closely with the peaks of this sample. The intensities of the peaks are lower than for all the previous samples. The broadening in the peaks is highest among all samples. The lattice constant for (101) and (002) planes is calculated to be 0.42196 nm and 0.65392 nm.

All major reflection peaks of the XRD patterns given from figures L<sub>x</sub> 1 to L<sub>x</sub> 9 could be indexed with the reported values in the JCPDS file of Lanthanum oxide and confirm the formation of hexagonal structure unit cell. There were six JCPDS files available for hexagonal structures. While the XRD patterns of the commercially available sample and the ones synthesized by the solid state method, furnace combustion method with fuel rich and fuel lean proportions and Co – precipitation method (L1, L2, L3, L5 and L9) match largely with JCPDS file 83 - 1355 of hexagonal structure having space group  $P6_3/mmc$ , the XRD patterns of samples synthesized by furnace combustion method with stoichiometric ratio and microwave combustion method with stoichiometric as well as fuel lean ratios match substantially with JCPDS file 74 – 2430 of hexagonal structure ( L4, L7 and L8) having space group  $P6_3/mmc$ . The XRD pattern of sample synthesized by microwave combustion method with fuel rich ratio (L6) matches well with JCPDS file 73 – 2141 of hexagonal structure with space group  $P3\bar{m}1$ . Many peaks observed in the XRD patterns of  $La_2O_3$  match closely with monoclinic and cubic structure.

L1	L2	L3	L4	L5	L6	L7	L8	L9
3.25935	3.39834	3.26266	3.25851	3.63694	3.64849	3.66255	4.32695	3.26989
3.18101	3.26617	3.18275	3.17808	3.27146	2.94663	3.27639	3.71733	3.19213
2.82245	3.05577	2.82632	3.01840	2.94018	2.10633	2.95654	3.38490	2.27967
2.27731	2.97081	2.27793	2.27466	2.10182	2.06145	2.36340	2.97515	2.12732
2.13413	2.27353	2.13407	2.13393	2.05802	1.94083	2.11241	2.66310	2.04152
1.86796	1.96372	1.86993	1.86803	1.93727	1.71337	1.94559	2.35723	1.87315
1.65917	1.74881	1.65856	1.65742	1.70990	1.61033	1.83098	2.08249	1.45193
1.45126	1.48648	1.45182	1.45040	1.51362	1.47305	1.71902	2.02147	
1.34708	1.30602	1.34653	1.34588	1.32698	1.32899	1.61185	1.69871	
							1.32232	

**Table 1:** *d* values of samples for closely matching peaks of the respective JCPDS files

Table 1 contains the *d* values of such peaks which closely match with the *d* values of a particular JCPDS file, as mentioned earlier. Since there are several reported structures for  $\text{La}_2\text{O}_3$  and at the same time, there are several peaks for each sample, it is manually difficult to get an authentic match. Hence, the numerical method of co-relation function was utilized to get the nearest match. The procedure was carried out using the co-relator available in mathematica. A typical calculation sheet is shown here for sample L1.

ah={3.5134,3.215,3.0832,2.3718,2.0285,1.8297,1.7567,1.7155,1.6946,1.6075,1.5416,1.4617,1.3586,1.3279,1.3005,1.2598,1.2273};  
bh={6.403,3.4978,3.2015,3.0696,2.3616,2.1343,2.0195,1.9259,1.8219,1.7489,1.708,1.6871,1.6007,1.5348,1.4669,1.4555,1.3527};

ch={6.1361,3.4105,3.068,2.9809,2.2809,2.0453,1.969,1.8748,1.7541,1.7052,1.6571,1.6429,1.534,1.4904,1.4185,1.399,1.3097};

dh={3.4098,3.0649,2.9798,2.2794,1.9686,1.7527,1.7049,1.6564,1.6425,1.5324,1.4899,1.3977,1.309,1.2887,1.2612,1.2092,1.188};

eh={6.12,3.4034,3.06,2.9744,2.2755,2.04,1.965,1.8709,1.7497,1.7017,1.6534,1.6395,1.53,1.4872,1.4152,1.3954,1.3067};

fh={6.13,3.4121,3.065,2.9813,2.2801,2.0433,1.97,1.8755,1.753,1.706,1.6572,1.6436,1.5325,1.4906,1.4182,1.3979,1.3096};

l1={3.25935,3.18101,2.82245,2.49043,2.27731,2.13413,1.9269,1.86796,1.82418,1.65917,1.63093,1.59192,1.56726,1.45126,1.34708,1.32614,1.30};

Correlation [l1, ah]

Correlation [l1, bh]

Correlation [l1, ch]

Correlation [l1, dh]

Correlation [l1, eh]

Correlation [l1, fh]

0.984674

0.883287

0.886173

0.983656

0.886265

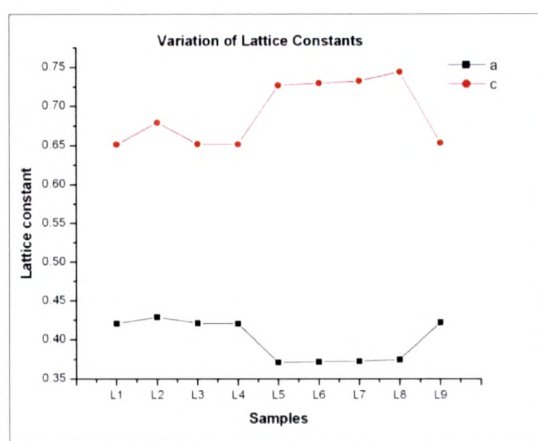
0.886413

0.983546

Within the samples that adhere to a particular JCPDS file, there are slight deviations in the d values. This shows that the structural properties of  $\text{La}_2\text{O}_3$  are sensitive to the process of synthesis and synthesis parameters. However, it needs to be ascertained whether this difference in d values is due to the structural properties or distortions in the lattice.

The Structural parameters like lattice constants and lattice volume are given in Table 2. The variation of lattice constants for the different samples is graphically presented below the table. The value of both the lattice constants remain similar for samples L1, L2, L3, L4 and L9, averaging 0.42255 and 0.65792 for a and c respectively. Such similarity of values is also observed for samples L5, L6, L7 and L8, where they average around 0.37256 and 0.73348 for a and c respectively. While the value of lattice constant a decreases in case of L5, L6, L7 and L8, an increase is seen in the value of lattice constant c for these samples. Small variations are observed within the groups having identical values of lattice constants. The

trends are by and large concurrent with observations mentioned earlier. The samples L1, L2, L3, L5 and L9 match with a single JCPDS file, while samples L4, L7, L8 and L6 match with other two files. However, all the samples fall under the hexagonal structure. The above facts again support the view that the structural parameters are sensitive to the synthesis techniques and synthesis parameters. The small variations are very likely due to the distortions in the lattice which might be either on account of the synthesis parameters or reduction in size of the crystallites leading to additional strain.



Good amount of broadening in the peaks is observed for samples synthesized by combustion method and co - precipitation method compared to samples synthesized by solid state and commercially available sample. From the broadening of the peaks, size of crystals can be measured by Scherer formula (discussed in Chapter2). The calculation of crystallite size by graphical method has also been undertaken. A typical data for determining crystal size by removing the strain is given in **Table 3**.

Parameters for Planes (101) and (002) of $\text{La}_2\text{O}_3$				
Sample	$d$ spacing nm	Lattice constant $a$ nm	Lattice constant $c$ nm	Volume $(\text{nm})^3$
L9	0.31900	0.42196	0.65392	0.100829
L8	0.29743	0.37465	0.74442	0.0904873
L7	0.29534	0.37267	0.73245	0.0880937
L6	0.29459	0.37179	0.72989	0.0873717
L5	0.29397	0.37113	0.72718	0.0867385
L4	0.31772	0.42018	0.65169	0.0996391
L3	0.31827	0.42090	0.65247	0.100101
L2	0.29707	0.42889	0.67967	0.10827
L1	0.31810	0.42082	0.65187	0.0999704

**Table 2:** Lattice constants and cell volume

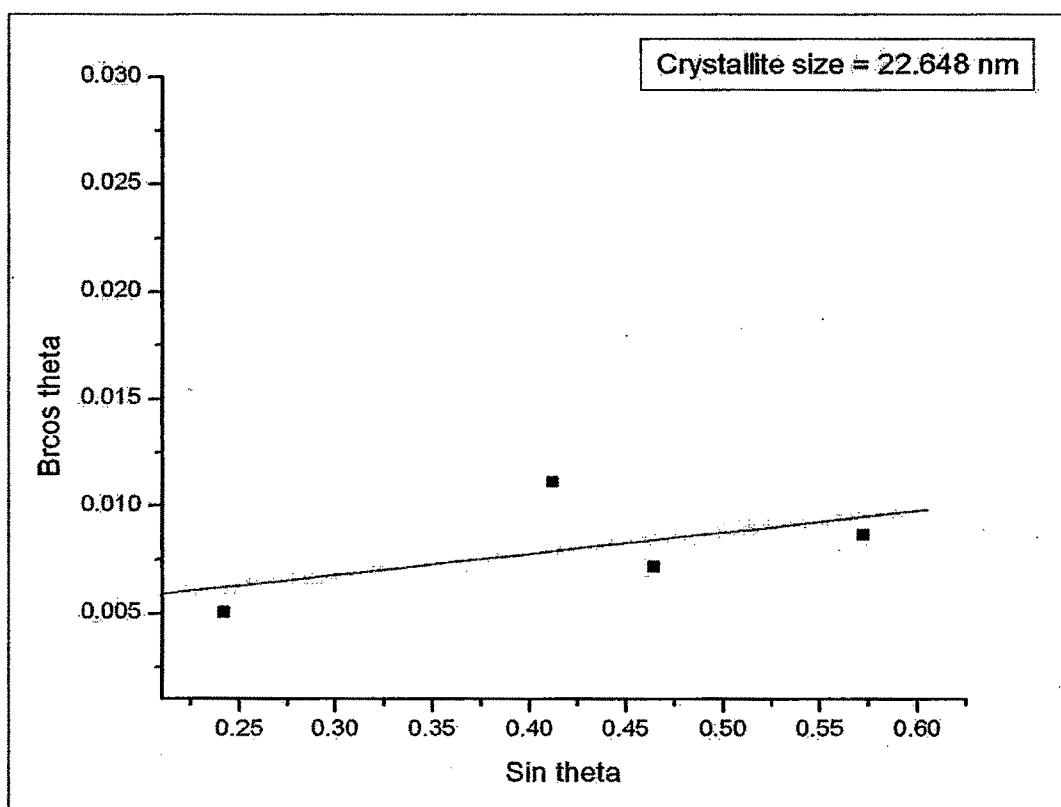
$2\theta$ values	FWHM	Silicon $2\theta$ values	Silicon FWHM	$B_i^2$	$B_o^2$	$B_r = \sqrt{B_o^2 - B_i^2}$	$\sin \theta$	$B_r \times \cos \theta$
30.011	0.351	28.370	0.1145	$3.993 \times 10^{-6}$	0.00003753	0.005791	0.258912	0.005594
44.799	0.339	47.238	0.1096	$3.659 \times 10^{-6}$	0.00003501	0.005599	0.381062	0.005176
53.932	0.370	56.060	0.1076	$3.526 \times 10^{-6}$	0.00004170	0.006179	0.453462	0.005507
71.258	0.466	69.078	0.1135	$3.924 \times 10^{-6}$	0.00006615	0.007888	0.582534	0.006412

**Table 3 :** Data for determination of crystallite size by graphical method for a typical sample  
(prepared by Microwave method)

## Sample L3

## Crystallite Size by Scherrer Formula

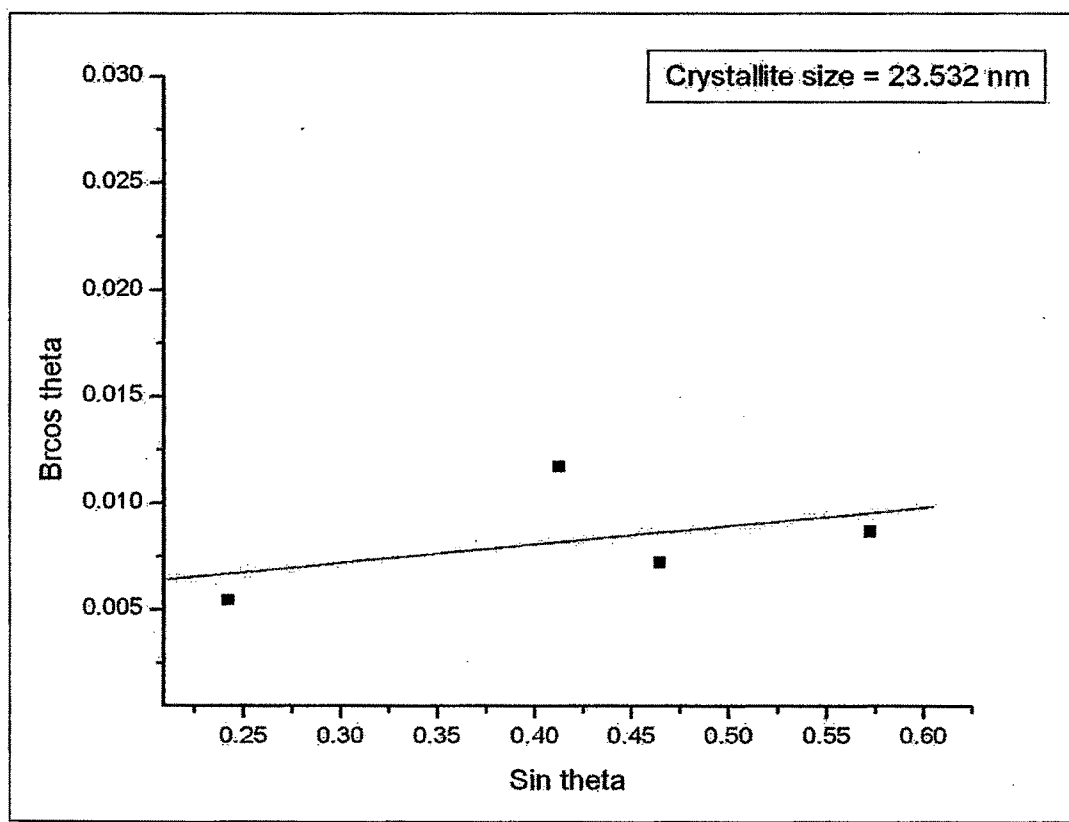
d values (°A)	Crystallite Size (nm)
3.26266	23.1817
3.18275	24.0872
2.82632	19.1562
2.27793	16.395
2.13407	13.8996
1.86993	10.2242
1.65856	14.7491
1.45182	11.7928
1.34653	10.5776
<b>Average Crystallite Size</b>	<b>16.0071</b>



## Sample L4

## Crystallite Size by Scherrer Formula

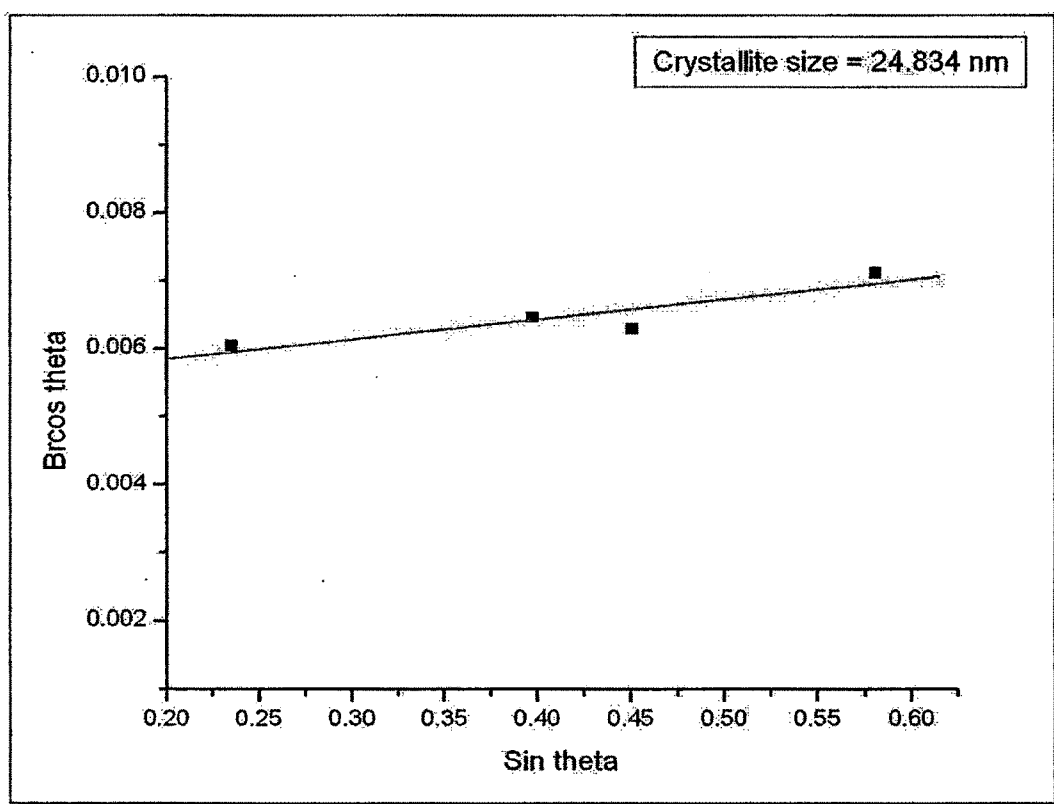
d values (°A)	Crystallite Size (nm)
3.25851	20.9185
3.17808	22.5357
3.01840	17.3779
2.27466	19.5162
2.13393	9.70139
1.86803	14.6542
1.65742	11.5854
1.45040	10.5409
1.34588	15.2437
<b>Average Crystallite Size</b>	<b>18.0202</b>



## Sample L5

## Crystallite Size by Scherrer Formula

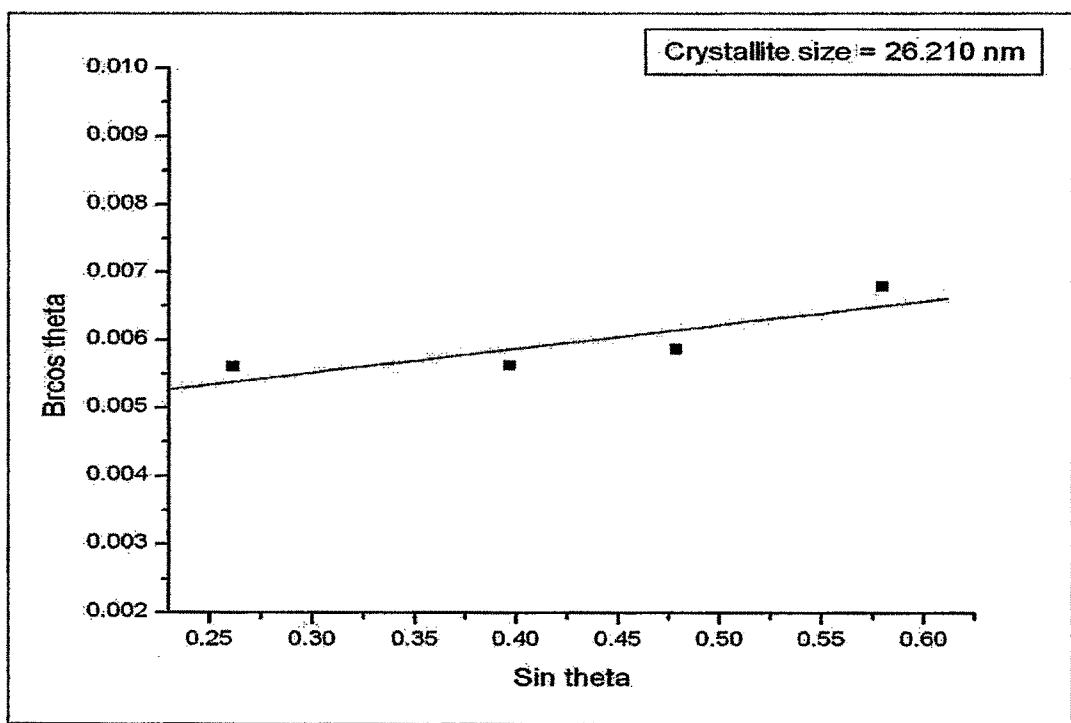
d values (°A)	Crystallite Size (nm)
3.63694	21.3293
3.27146	20.6436
2.94018	22.417
2.10182	20.8207
2.05802	17.4565
1.93727	17.438
1.70990	16.9672
1.51362	12.5246
1.32698	12.5848
<b>Average Crystallite Size</b>	<b>15.786</b>



## Sample L6

## Crystallite Size by Scherrer Formula

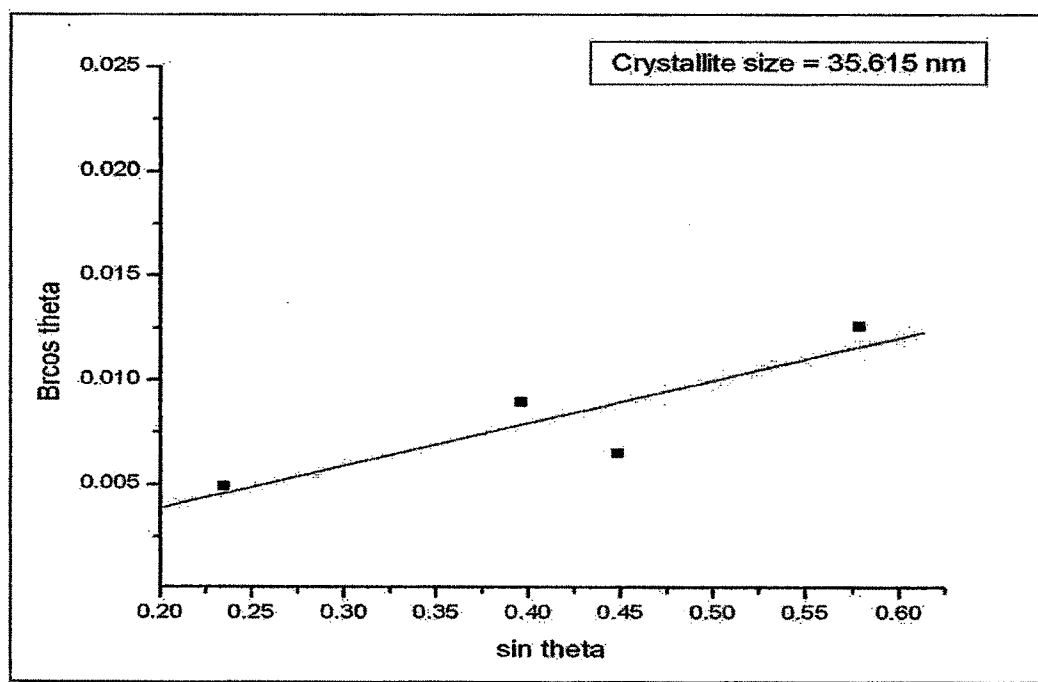
d values (°A)	Crystallite Size (nm)
3.64849	25.5431
2.94663	21.7832
2.10633	23.6981
2.06145	20.0781
1.94083	19.814
1.71337	18.3367
1.61033	17.5287
1.47305	16.1608
1.32899	13.1849
<b>Average Crystallite Size</b>	<b>19.5697</b>



## Sample L7

## Crystallite Size by Scherrer Formula

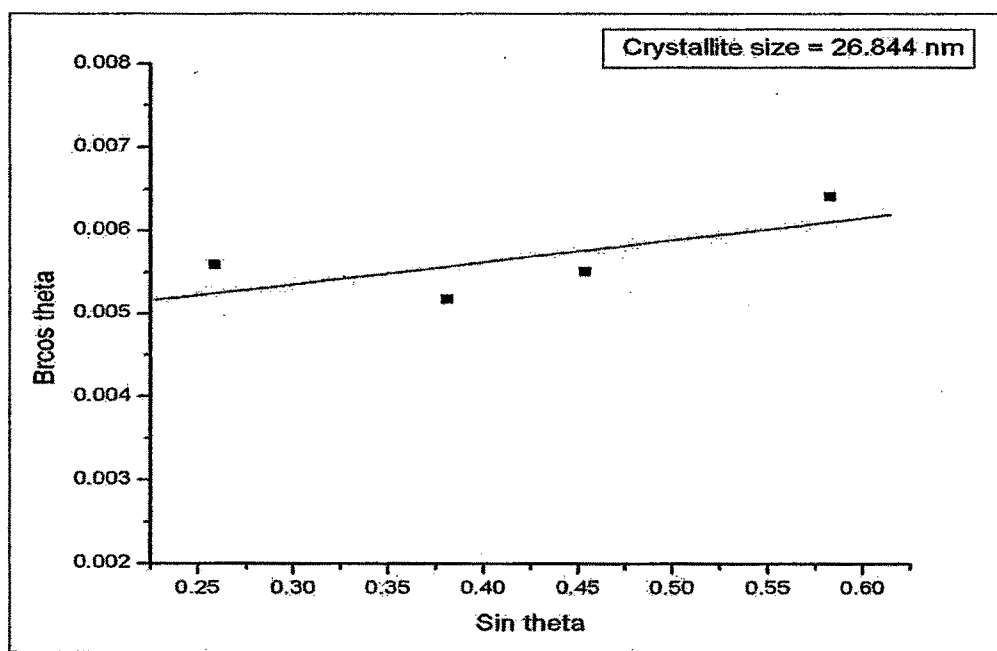
d values ( $^{\circ}\text{A}$ )	Crystallite Size (nm)
3.66255	14.8213
3.27639	24.8275
2.95654	11.2286
2.36340	21.336
2.11241	21.6282
1.94559	12.7745
1.83098	14.9205
1.71902	16.5159
1.61185	10.1142
<b>Average Crystallite Size</b>	<b>20.1581</b>



## Sample L8

## Crystallite Size by Scherrer Formula

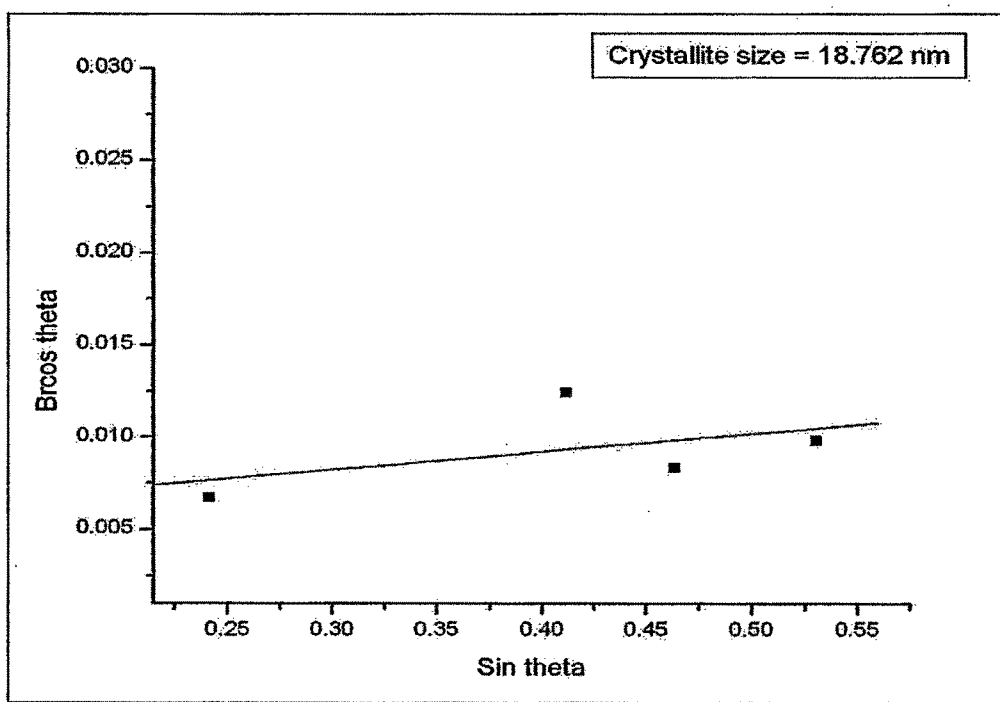
d values (°A)	Crystallite Size (nm)
4.32695	21.8969
3.71733	14.8314
3.38490	23.802
2.97515	21.861
2.66310	22.3662
2.35723	18.3569
2.08249	23.8085
2.02147	21.6658
1.69871	19.1361
1.32232	13.8562
<b>Average Crystallite Size</b>	<b>16.463</b>



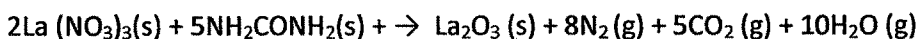
## Sample L9

## Crystallite Size by Scherrer Formula

d values (°A)	Crystallite Size (nm)
3.26989	20.4245
3.19213	18.6659
2.27967	11.4856
2.12732	11.7905
2.04152	12.6409
1.87315	9.18746
1.45193	10.0064
<b>Average Crystallite Size</b>	<b>13.4573</b>



The reaction between Lanthanum Nitrate and Urea, which is exothermic in nature, is given below.



The reaction becomes vigorous with large amount of gas released. 23 moles of gas is released per mole of  $\text{La}_2\text{O}_3$  formed. The heat of combustion of Lanthanum nitrate is quite high but not as high as  $\text{CeO}_2$ , where the reaction is more vigorous. The flame temperature is generally highest in samples synthesized by stoichiometric ratio compared to fuel deficient and fuel rich ratios. As discussed in Chapter 4, Urea on heating decomposes into biuret and ammonia initially and at higher temperatures to  $(\text{HNCO})_3$  trimer. On the other hand,  $\text{La}(\text{NO}_3)_3$  <sup>[23]</sup> melts on heating followed by dehydration and decomposition to amorphous  $\text{La}_2\text{O}_3$  and oxides of nitrogen. However, Lanthanum nitrate - Urea mixtures when heated are reported <sup>[24]</sup> to form  $\text{La}(\text{OH})(\text{NO}_2)_2$  gel. Thus, during the combustion of Lanthanum nitrate - urea mixtures, all these reactions appear to occur simultaneously forming a polymeric gel which foams by the large amounts of gases produced. The appearance of a flame may be attributed to the gas phase reactions in the form of combustible gases like ammonia and cyanic acid with oxides of nitrogen. Ammonia-nitrogen oxide flames are known to give a flame having a temperature of  $\approx 2000^\circ\text{C}$ . Thus, production of high temperatures ( $>1100^\circ\text{C}$ ) on account of combustion is a certainty during the process of reaction, though the temperatures were not measured.

Combustion process can give different phases in a structure of a material depending upon the fuel to oxidant ratio, type of fuel used etc <sup>[25]</sup>. When combustion process is carried out with fuel lean ratio then the amount of Urea available is less compared to metal nitrates. Oxidizing environment is created and phases which are thermodynamically favoured in this environment get formed. When combustion is carried out with fuel rich ratio the amount of Metal nitrates available are less compared to Urea and reducing environment is created. The combustion synthesis of Copper nitrate with glycine produced Copper metal when the condition was fuel rich. Fuel lean condition produced mostly copper oxide with small

amount of  $\text{Cu}_2\text{O}$  and stoichiometric condition gives all the three phases of Copper, Copper oxide and  $\text{Cu}_2\text{O}$ . The presence of all the three phases indicates that the product was not in the equilibrium state <sup>[26]</sup>. The rapid cooling in air which occurs as the process gets over, also affects the formation of phases. There may be some phases which are formed in fuel lean condition as they are energetically favoured in this condition while some phases are formed in fuel rich condition. Similar phenomenon is observed in the combustion synthesis of BAM:  $\text{Eu}^{2+}$  <sup>[27]</sup>. In fuel lean condition, oxidation will take place very strongly as lots of oxygen is available from oxidizer and from the air as well. All the available form of metal oxides can be formed. In fuel rich condition, the oxygen available is very less and the metals get reduced <sup>[26]</sup>. There may be some phases of oxides of lanthanum with valency +2 like  $\text{LaO}$  in fuel lean condition. There may be some intermediate phases present in samples synthesized with stoichiometric ratio <sup>[28]</sup>. Barium carbonate is a dominant phase when  $\text{YBa}_2\text{Cu}_3\text{O}_{7-x}$  is synthesized by combustion method with stoichiometric ratio <sup>[27]</sup>. There may be some phases present due to impurities of Carbon <sup>[25]</sup> in the material synthesized in fuel rich condition because of the presence of Urea. Besides, there may be additional phases present due to structural difference in the  $\text{La}_2\text{O}_3$ . As the symmetry of the crystal decreases there is an increase in number of phases formed <sup>[29]</sup>. The structure of  $\text{La}_2\text{O}_3$  may be altogether different from the hexagonal, monoclinic or cubic structures discussed above. Due to the lack of standard patterns, formation of other structures like rhombohedral, triclinic etc could not be ascertained. The additional phases observed in almost all the samples of  $\text{La}_2\text{O}_3$  may be due to this reason. From the above results, it is indicated that  $\text{La}_2\text{O}_3$  prepared by combustion method may not be in equilibrium state.

The above discussions point out to the possibility that when the sample is synthesized in fuel lean condition then the formation of possible extra peaks are of  $\text{LaO}_2$ , as  $\text{La}^{3+}$  may get oxidized to  $\text{La}^{4+}$  and  $\text{La}(\text{NO})_3$ , as excess unreacted nitrate may be present. For samples synthesized in stoichiometric condition, formation of possible phases may be due to Lanthanum Nitrate <sup>[27]</sup>, La metal,  $\text{LaO}$ ,  $\text{LaO}_2$  and some intermediate phases. For sample

synthesized in fuel rich condition, formation of possible phases is due to La metal, LaO and due to the carbon as impurity.

Same situation is observed for the samples synthesized by Co –Precipitation method and solid state synthesis method. For samples synthesized by solid state synthesis method, number of phases formed is less and the peak intensity is very high compared to Co –precipitation method. In fact the intensity of these peaks of solid state synthesized samples is higher than all the samples synthesized by combustion method ensuring very good crystallinity. Thus it can be said that the structural symmetry and stability is highest for solid state synthesized samples and lowest for samples synthesized in fuel lean condition for microwave combustion synthesis as can be seen from figure L<sub>x</sub> 2 and L<sub>x</sub> 8.

For the combustion synthesis process of Lanthanum Oxide, it is observed that the average crystallite size increases in the order from fuel lean ratio to fuel rich ratio to stoichiometric ratio for both furnace and microwave combustion synthesized samples. As discussed in Chapter 4 for Ceria, two major competing events namely high flame temperature and evolution of large amount of gas takes place during combustion process. Though highest flame temperature is attained for stoichiometric ratio, the flame temperature is relatively low, as the combustion process proceeds at slower rate and a large amount of gas is released reducing the flame temperature. This low flame temperature in samples with fuel rich ratio is responsible for smaller crystallite size compared to samples synthesized with stoichiometric ratio. In fuel lean condition, the combustion may be incomplete as the amount of fuel available is less. No flame is observed but the amount of gas released is very high and the combustion process gets over within a very short period of time compared with other two ratios. So the crystallite size is smallest here. The intensity of the peaks is less for the fuel lean ratios because their crystallinity is not good compared to the material synthesized by other two ratios. There may be some amount of amorphicity present as the process of combustion is not complete.

In microwave combustion (Chapter 4) the heat is generated within the sample by interaction of microwaves with the material. When the microwaves penetrate and propagate through a dielectric material, the internal electric field generated within the affected volume induce translational motion of free or bonded charges and also rotate complexes such as dipoles. The resistance of these induced motions due to internal elastic and frictional forces, which are frequency dependent, cause losses and attenuate the electric field. As a result volumetric heating occurs <sup>[30]</sup>. In conventional heating, the heat generated by heating elements is transferred to the sample surface, and then transferred to the interior by conduction. Hence, it is expected that the crystallites synthesized by microwave combustion method should be smaller than crystallites synthesized by conventional furnace combustion method. In the case of combustion of Lanthanum nitrate - urea mixtures to give  $\text{La}_2\text{O}_3$ , contrary effect is observed i.e. the crystals synthesized are larger for microwave combustion method than furnace combustion method. This may be due to marked difference in the decomposition/combustion behavior of the precursors i.e. Lanthanum precursors burn/decompose with swelling initially and there is a persistent flame observed. This flame remains for longer duration in microwave combustion method, which may be due to internal heating <sup>[31, 32]</sup>. The absorption of microwaves by the material is a characteristic property of the material <sup>[33]</sup>. It may be possible that Lanthanum nitrate absorbs microwaves very strongly and the internal heating process may be quite intense compared to the heating in furnace combustion process. The exact reason still needs to be investigated further. The average crystallite sizes are found to be smallest for samples synthesized by Co – precipitation method. This is because the heat available for the crystal growth is minimal and the agglomeration is also minimum as described in Chapter 4 for Ceria.

The average crystallite size is found to be minimum in sample synthesized by co – precipitation method. It is found to be maximum in samples synthesized with stoichiometric ratios in microwave and furnace combustion method followed by fuel lean and fuel rich ratios. The rapid combustion and quenching of reaction from very high temperature to

room temperature induces additional surface and bulk defects<sup>[34]</sup> which may be the cause of strain in the samples.

### **Scanning Electron Microscopy**

Scanning Electron Microscopy (SEM) was done for samples prepared by solid state, combustion (furnace and microwave) and co-precipitation synthesis methods. The SEM was done of JEOL make JSM 5610 LV Scanning Electron Microscope.

The micrograph of the sample prepared by solid state synthesis is given in figure L<sub>S</sub> 1. The SEM micrograph was taken with accelerating voltage of 15 KV and magnification of 10,000. The image was formed by secondary electron signal. The particles are coarse and highly agglomerated. The particles are in irregular shape with rough edges. The grain growth is highly exaggerated with the sizes of the micrometer order. The agglomeration is due to the heat available for long time which causes the crystal to grow larger and agglomerate. Size distribution is very large. The structure is observed to be pore free.

Scanning electron micrograph of sample prepared by furnace combustion in stoichiometric ratio is given in figure L<sub>S</sub> 2. The SEM micrograph was taken with accelerating voltage of 15 KV and magnification of 20,000. The microstructure is observed to be fine grained. The agglomeration is very high and the structure is highly dense. The nature of the product is quite foamy, fluffy and voluminous. The surface is rough with large amount of pores and voids seen. The porosity is due to the large amount of gas escaping during the combustion reaction. The image reveals non-uniform particles which are soft agglomerates.

For the sample prepared by microwave combustion in stoichiometric ratio, the micrograph is given in figure L<sub>S</sub> 3. The SEM micrograph was taken with accelerating voltage of 15 KV and magnification of 5000. Here too, the non uniformity of grain growth is revealed. The particles are fine and highly agglomerated dense structures. A continuous network of

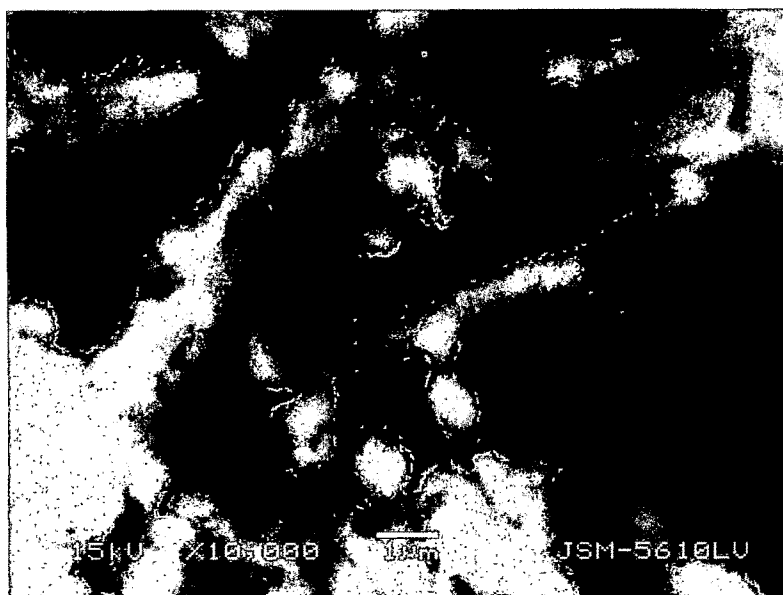


**Figure L<sub>5</sub> 1** Scanning Electron Micrograph of La<sub>2</sub>O<sub>3</sub> synthesized by Solid State Synthesis

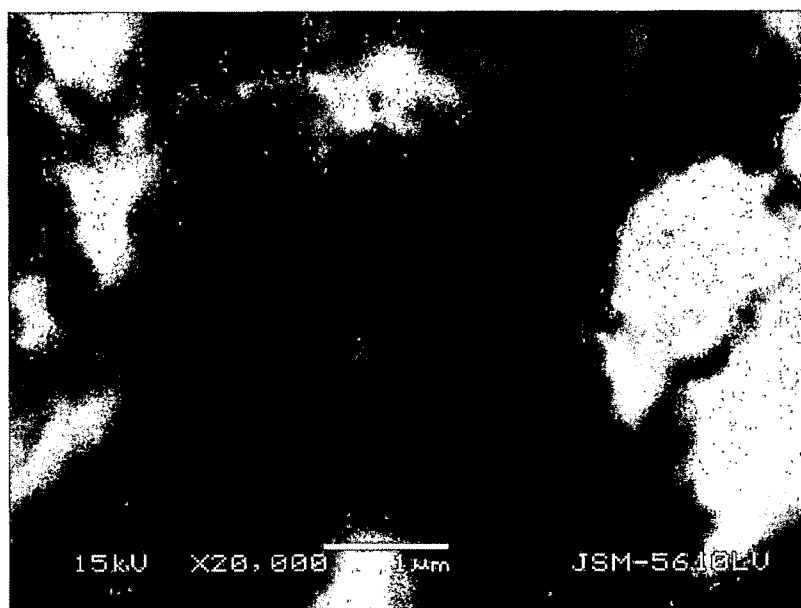


**Figure L<sub>5</sub> 2** Scanning Electron Micrograph of La<sub>2</sub>O<sub>3</sub> synthesized by Furnace Combustion

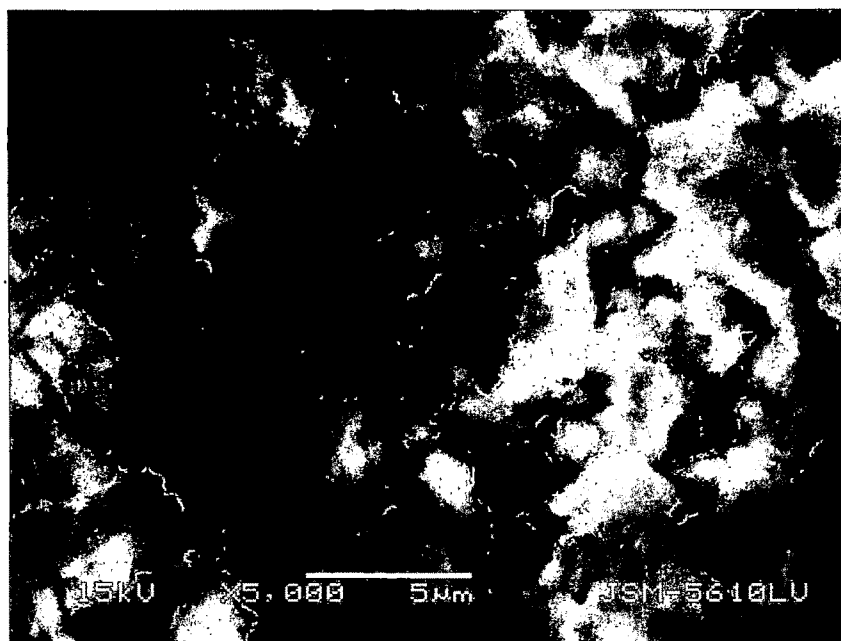


**Figure L<sub>5</sub> 3** Scanning Electron Micrograph of Stoichiometric  $\text{La}_2\text{O}_3$  synthesized by Microwave Combustion

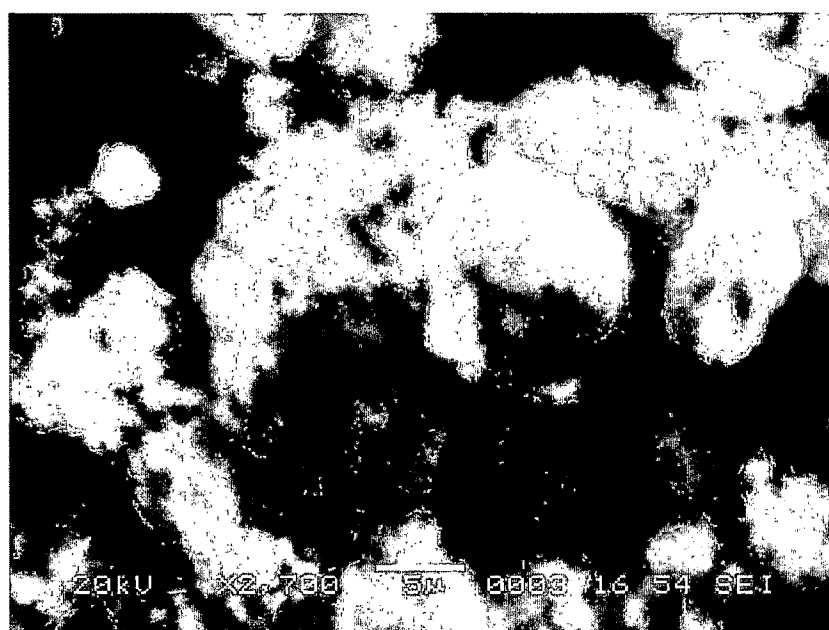


**Figure L<sub>5</sub> 4** Scanning Electron Micrograph of Stoichiometric  $\text{La}_2\text{O}_3$  synthesized by Co-precipitation

powders is seen to be formed with layers of agglomerates sticking together. The primary particles get agglomerated to form larger particles. The porosity observed in the sample is less compared to the sample in figure L<sub>5</sub> 2, probably due to the internal mode of heating. The agglomerates appear to be hard. In both the images the surface area of the particle is quite high.

The SEM micrograph of powders prepared by Co-precipitation is given in figure L<sub>5</sub> 4. The SEM micrograph was taken with accelerating voltage of 20 KV and magnification of 2,700. The particles are very fine and soft in nature. The extent of agglomeration is high but it is low compared to samples synthesized by Furnace and microwave combustion and Solid state synthesis. The image resembles that of cotton. Here also the surface area of the particle is high.

There is a good amount of agglomeration seen in the structures which may be attributed to the fineness of the particles. Due to high surface to volume ratio, the surface effects come into play which may be the cause of the agglomeration. Flame temperature plays a dominant role for samples prepared by microwave combustion with stoichiometric ratio as the product is hard agglomerate and not foamy and less porous in nature.

#### **Fluorescence Characteristics:**

The fluorescence characteristics of the samples were recorded on a *Fluoromax 4* instrument of *Horiba Jobin Yvon* make, USA. Equal amount of samples were taken in each case. The slit width for the excitation as well as emission monochromators was fixed at 1 nm to ensure optimization and uniformity. The integration time was kept at 0.1 second.

To begin with, a random check was carried out for the emission lines. These emission lines were then used to get the exact excitation features. The reported emission spectra were

taken for these precise excitation wavelengths. Thereafter, the excitation spectra were recorded for the obtained emission lines. The results are as under.

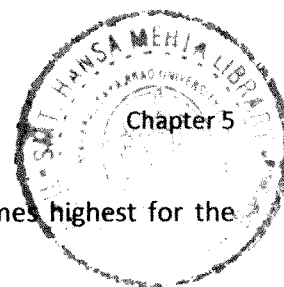
### **La<sub>2</sub>O<sub>3</sub>: Eu<sup>3+</sup>**

Figure LEF1b shows emission spectra of sample L2 synthesized by solid state synthesis, for four different excitation wavelengths 293, 395, 466 and 538 nm. Eight major and minor emission peaks are observed with the peak at 624 nm having the highest intensity followed by peaks at 612, 595, 587, 706, 579, 684 and 650 nm in the order of decreasing intensities. The intensities of the emission peaks are highest for excitation wavelength 293 nm followed by 395, 466 and 538 nm respectively.

Figure LEF1a shows excitation spectra of sample L2. The excitation spectrum was recorded for five different emission wavelengths 587, 595, 612, 624 and 706 nm. There is one broad band and eight major as well as minor peaks. In general, the intensity of the broad band at 293 nm is highest followed by peaks at 395, 466, 362, 382, 538, 402, 532 and 414 nm in the decreasing order of intensities. The intensity of the broad band is highest for the emission wavelength 624 nm followed by 612, 595, 587 and 706 nm respectively.

Figure LEF2b shows emission spectra of sample L3 synthesized by furnace combustion method with fuel rich ratio. The emission spectrum has been recorded for four different excitation wavelengths 281, 394, 465 and 535 nm. Eight major peaks were observed. The peak at 611 nm has the highest intensity followed by peaks at 624, 590, 695, 689, 592 and 578 nm in the order of decreasing intensities. In general, the intensities of the emission peaks are highest for excitation wavelength 281 nm followed by excitation at 465, 394 and 535 nm respectively.

Figure LEF2a shows excitation spectra of sample L3 monitored for four different emission wavelengths 590, 611, 624 and 704 nm. There is one broad band and several major as well as minor peaks. The intensity of the broad band at 281 nm is highest followed by peaks at 465, 395, 535, 362, 415, 382, 402 and 526 nm in the decreasing order of intensities. The intensity of the broad band is highest for the emission wavelength 611 nm followed by 624,



590, and 704 nm. The intensity of the 395 nm excitation peak becomes highest for the emission line of 590 nm.

Figure LEF3b shows emission spectra of sample L4 synthesized by furnace combustion method with stoichiometric ratio for the excitation wavelengths 282, 395, 465 and 532 nm. Out of the observed peaks, the one at 614 nm has the highest intensity followed by peaks at 618, 578, 594, 703, 589 and 585 nm in the order of decreasing intensities. In general, the intensities of the emission peaks are highest for excitation wavelength at 282 nm followed by the excitations of 395, 465 and 532 nm respectively.

Figure LEF3a shows excitation spectra of sample L4 for the emission lines 578, 594, 614 and 704 nm. There is one broad band and seven major as well as minor peaks observed. The intensity of the broad band at 282 is highest followed by the peaks at 466, 395, 362, 532, 381 and 414 nm in the decreasing order of intensities. The intensity of the broad band is highest for emission wavelength 614 nm followed by those for 578, 594, and 704 nm respectively.

Figure LEF4b shows emission spectra of sample L5 synthesized by furnace combustion method with fuel lean ratio for four different excitation wavelengths 280, 395, 465 and 532 nm. There are seven major peaks with the peak at 618 nm having the highest intensity followed by peaks at 614, 578, 594, 704, 590 and 695 nm in the order of decreasing intensities. In general, the intensities of the emission peaks are highest for excitation wavelength at 465 nm followed by excitations at 395, 532 and 280 nm respectively.

Figure LEF4a shows excitation spectra of sample L5 for five different emission wavelengths 578, 594, 614, 618 and 704 nm. There is one broad band and six major as well as minor peaks. The intensity of the peak at 395 nm is highest followed by the peak at 465 nm, a broad band at 280 nm and other peaks at 381, 362 and 413 nm in the decreasing order of intensities. The intensity of the broad band is highest for the emission line 618 nm followed by those for 614, 578, 594, and 704 nm respectively. In general, the intensities of the peaks

is highest for emission wavelength at 618 nm followed by 614, 578, 594 and 704 nm respectively.

Figure LEF5b shows emission spectra of sample L6 synthesized by microwave combustion method with fuel rich ratio. The emission peaks are for four different excitation wavelengths 268, 362, 395 and 465 nm. The peak at 614 nm has the highest intensity followed by peaks at 618, 590, 593, 695, 680, 646 and 578 nm in the order of decreasing intensities. In general, the intensities of the emission peaks are highest for excitation wavelength 395 nm followed by excitations at 465, 362 and 268 nm respectively.

Figure LEF5a shows excitation spectra of sample L6 for five different monitoring wavelengths 590, 614, 618 and 695 nm. There is one broad band and several other peaks. The intensity of the peak at 395 is highest followed by peaks at 465, 414, 387, 362 and a broad band at 265 nm in the decreasing order of intensities. In general, the intensity of the excitation peaks is highest for emission wavelength 614 nm followed by those of 618, 590 and 695 nm respectively.

Figure LEF6b shows emission spectra of sample L7 synthesized by microwave combustion method with stoichiometric ratio for four different excitation wavelengths 260, 361, 395 and 465 nm. There are five major peaks with the peak at 617 nm having the highest intensity followed by the peaks at 591, 588, 690 and 646 nm in the order of decreasing intensities. In general, the intensities of the emission peaks are highest for excitation wavelength 395 nm followed with excitation by 465, 260 and 361 nm respectively.

Figure LEF6a shows excitation spectra of sample L7 monitored for three different emission wavelengths namely 590, 616 and 690 nm. The intensity of the peak at 395 nm is highest followed by peak at 465 nm, a broad band at 263 nm and peaks at 375, 361 and 414 nm in the decreasing order of intensities respectively. The intensities of the peaks are highest for emission wavelength 616 nm followed by emission lines 590 and 690 nm in that order.

Figure LEF7b shows emission spectra of sample L8 synthesized by Microwave combustion method with fuel lean ratio. The emission spectrum is for four different excitation wavelengths 257, 361, 394 and 463 nm. There are six significant emission peaks with the peak at 612 nm having the highest intensity followed by the intensities of the emission peaks at 620, 586, 592, 698 and 594 nm in the order of decreasing intensities. In general, the intensities of the emission peaks are highest for excitation wavelength 394 nm followed with excitations by 463, 361 and 257 nm respectively.

Figure LEF7a shows excitation spectra of sample L8 for emission wavelengths 587, 608, 612 and 698 nm. There is one broad band and six other peaks in the spectra. The intensity of the excitation peak at 394 is highest followed by intensities of peaks at 464, 382, 375, 361, 318 nm and a broad band at 254 nm in the decreasing order of intensities. The broad band is almost nonexistent. In general, the intensities of the peaks are highest for emission wavelength 612 nm followed by the intensities for the monitoring lines 608, 587 and 698 nm respectively.

Figure LEF8b shows emission spectra of sample L9 synthesized by co – precipitation for five different excitation wavelengths 285, 362, 395, 465 and 532 nm. There are eight major and minor peaks observed with the peak at 614 nm having the highest intensity followed by the peaks at 618, 578, 594, 584, 700, 704 and 696 nm in the order of decreasing intensities. The intensities of the emission peaks, in general, are highest for the excitation wavelength 285 nm followed by the excitations of 465, 395, 532 and 362 nm respectively.

Figure LEF8a shows excitation spectra of sample L8 monitored for three different emission wavelengths namely 578, 594, 614 and 704 nm. There is one broad band and six major peaks. The intensity of the excitation broad band at 285 nm is highest followed by peaks at 465, 395, 395, 532, 362, 380 and 414 nm in the decreasing order of intensities. The intensity of the broad band is highest for emission wavelength 614 nm followed by the intensities for 578, 594 and 704 nm respectively.

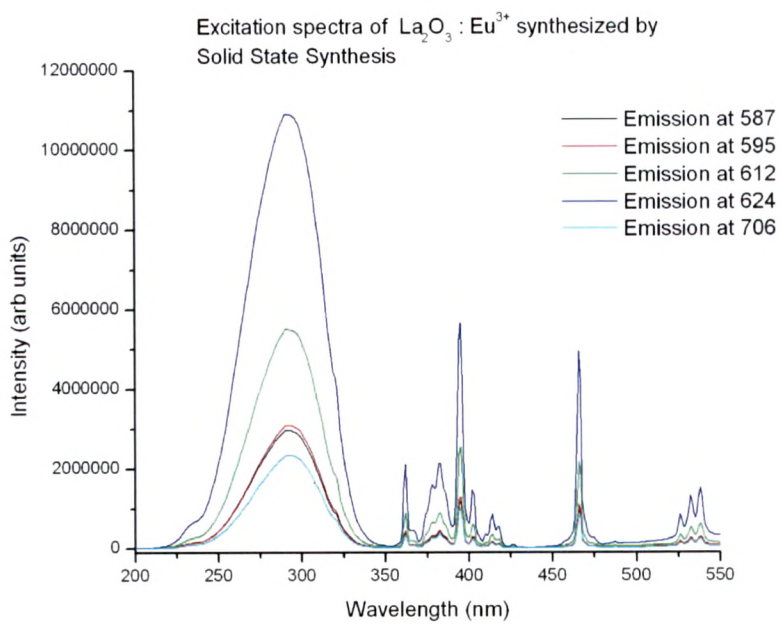


Figure: LEF1a

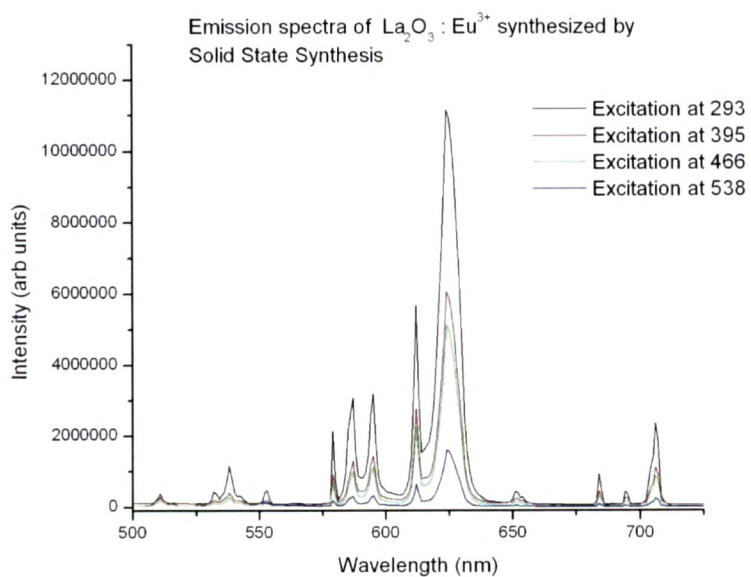


Figure: LEF1b

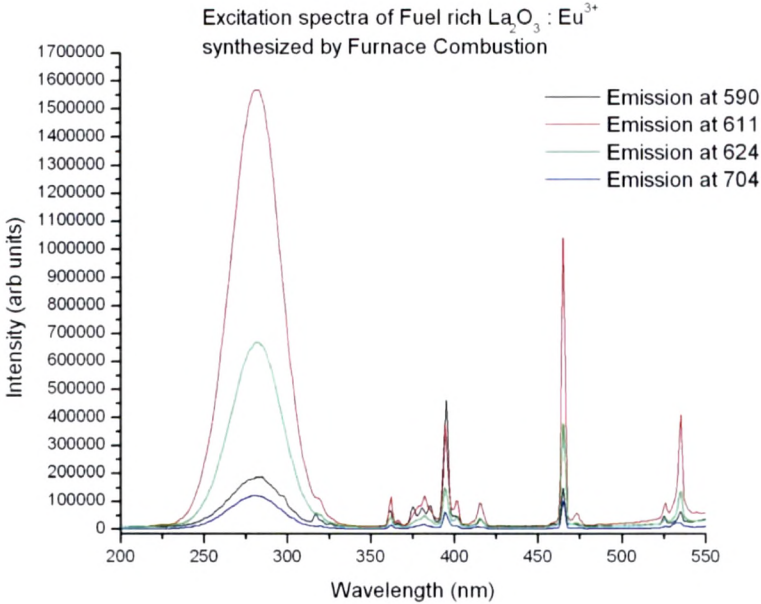


Figure: LEF2a

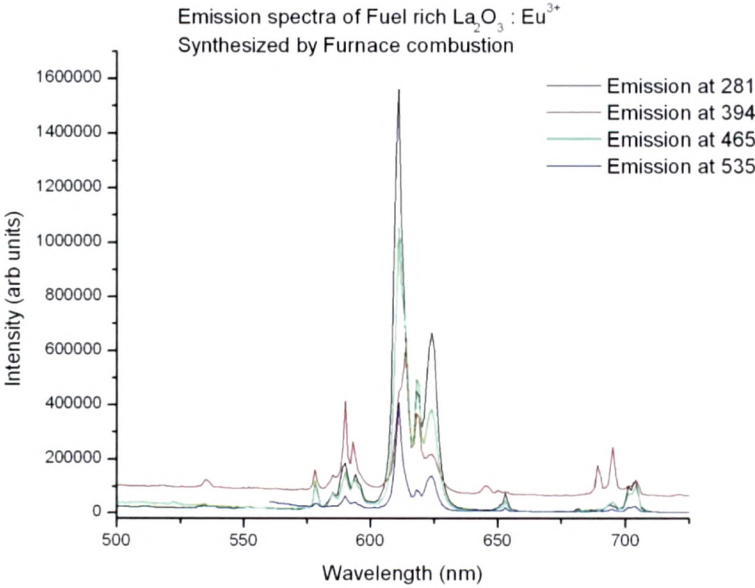


Figure: LEF2b

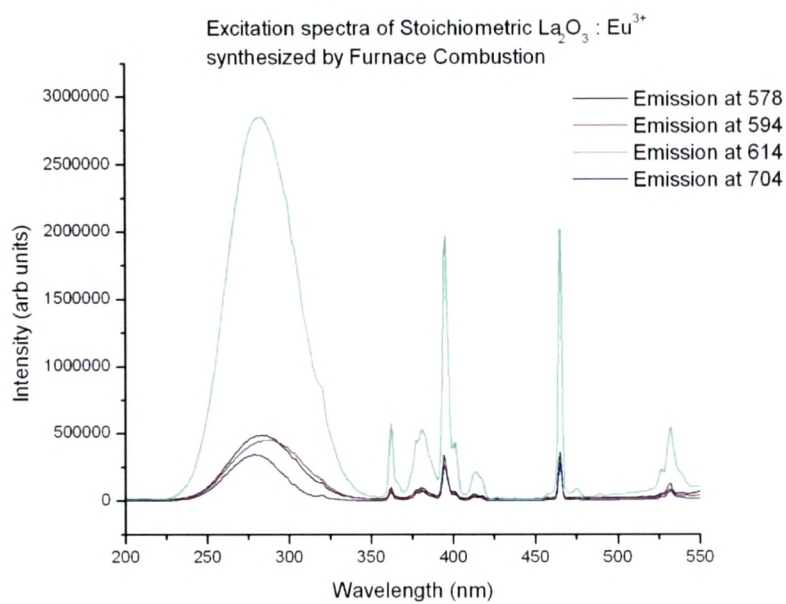


Figure: LEF3a

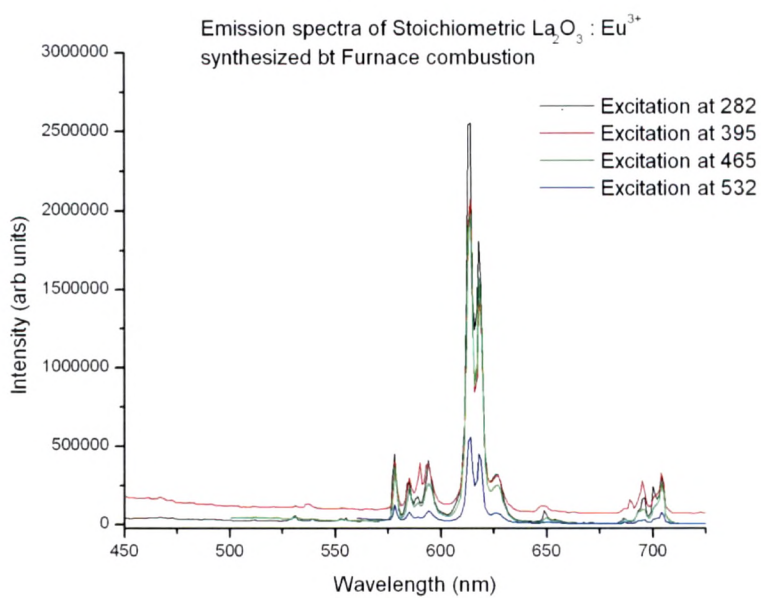


Figure: LEF3b

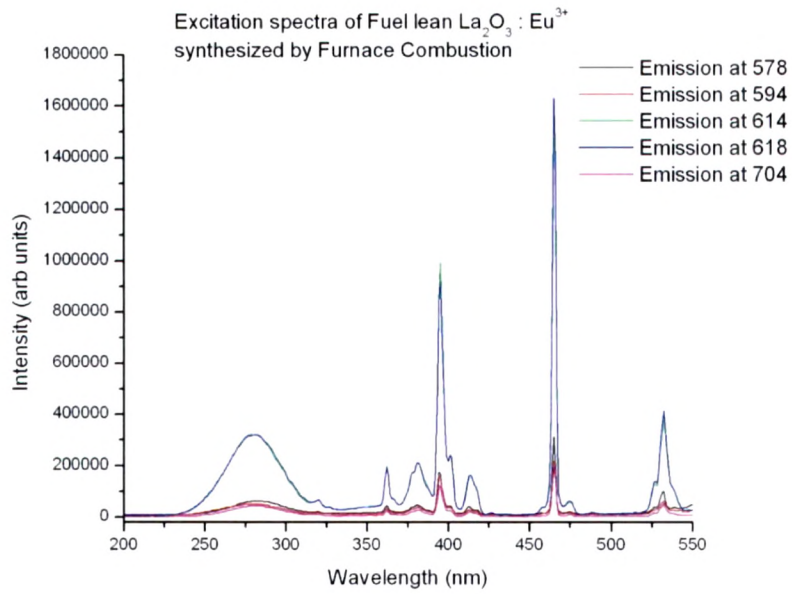


Figure: LEF4a

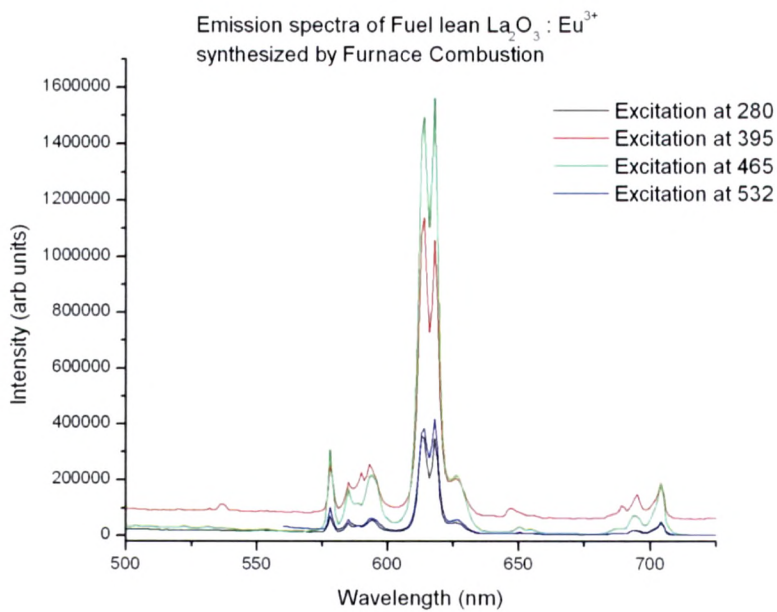


Figure: LEF4b

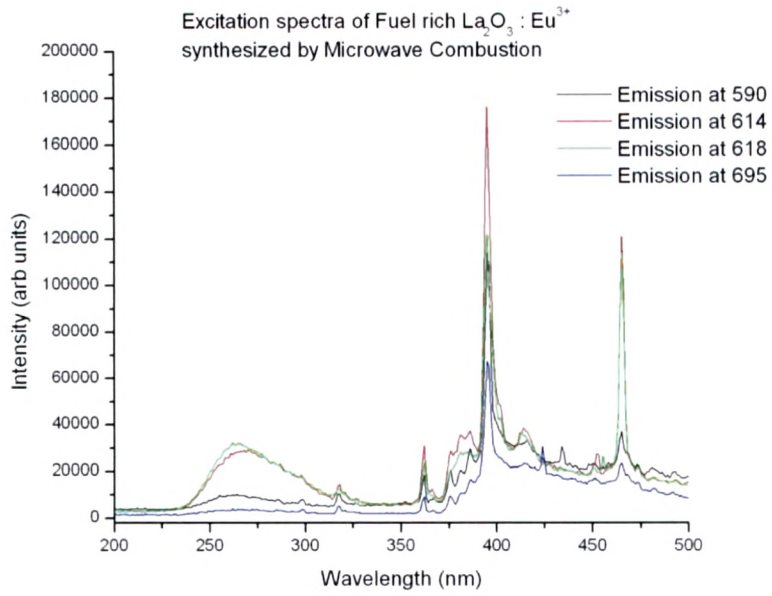


Figure: LEF5a

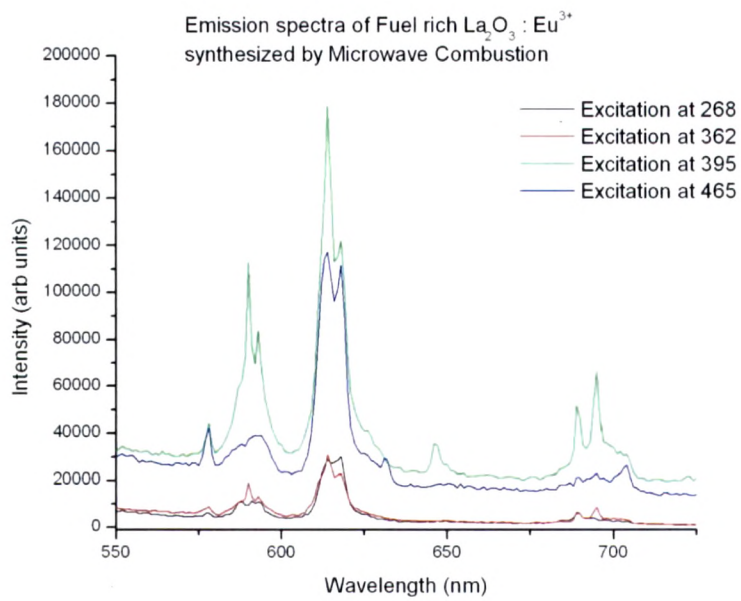


Figure: LEF5b

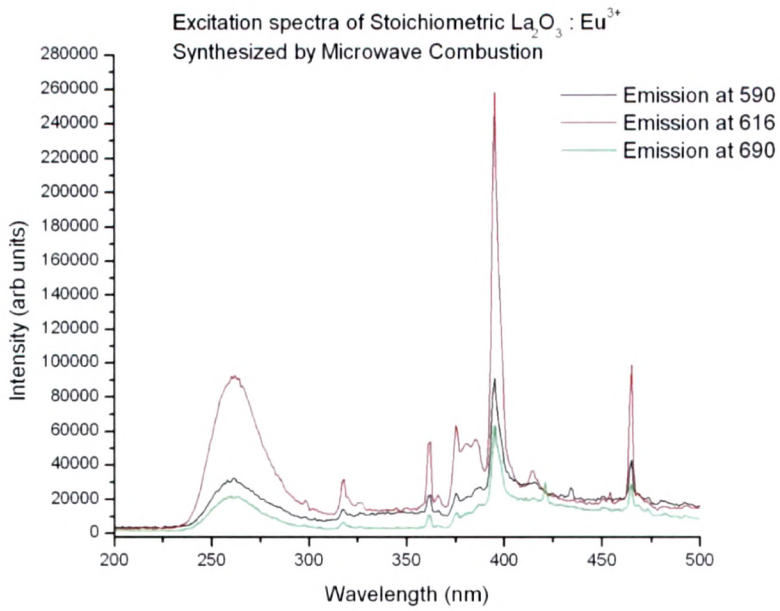


Figure: LEF6a

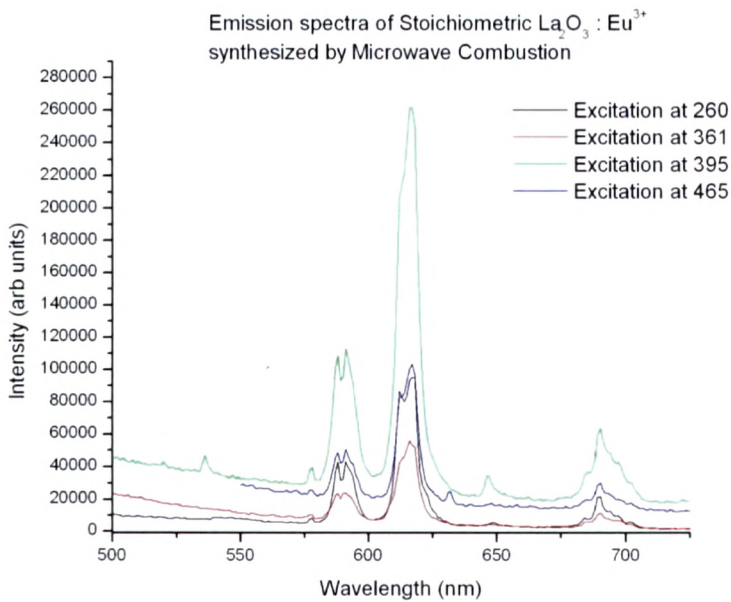


Figure: LEF6b

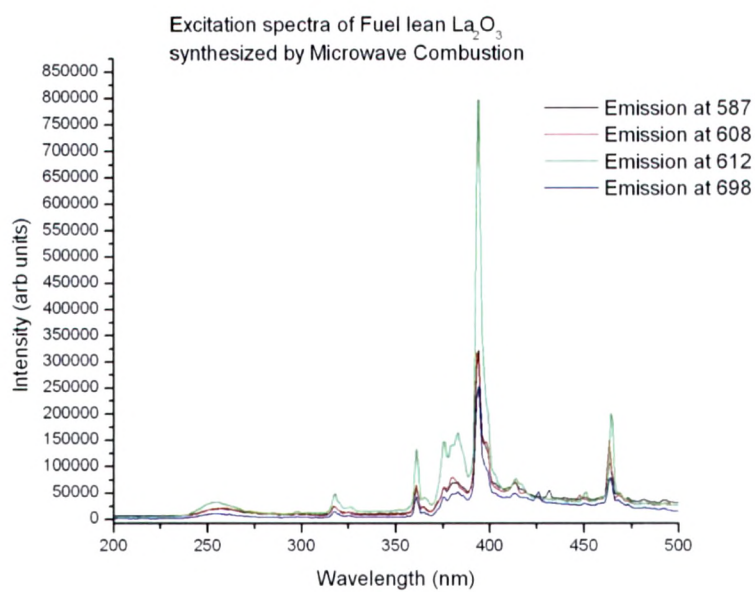


Figure: LEF7a

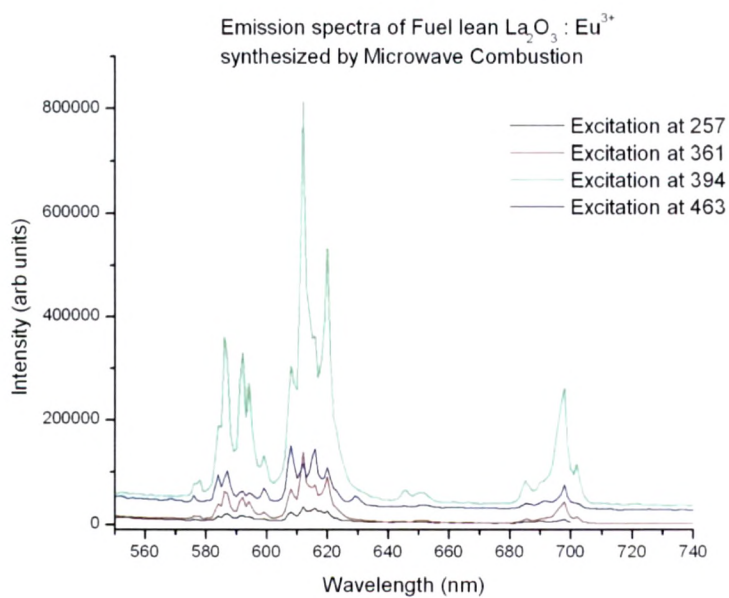


Figure: LEF7b

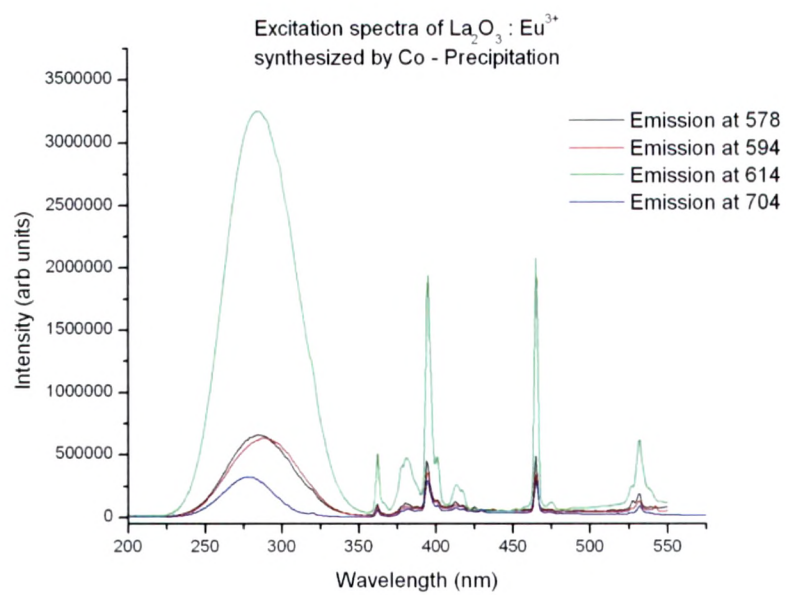


Figure: LEF8a

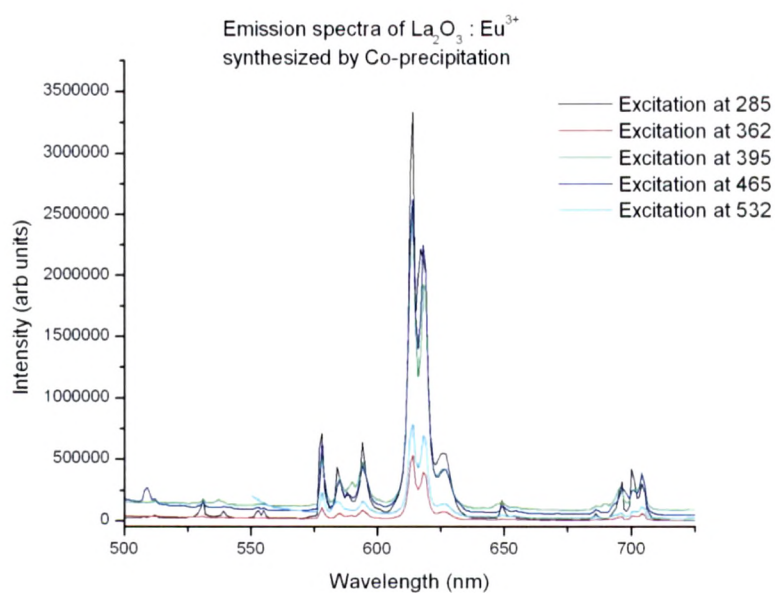
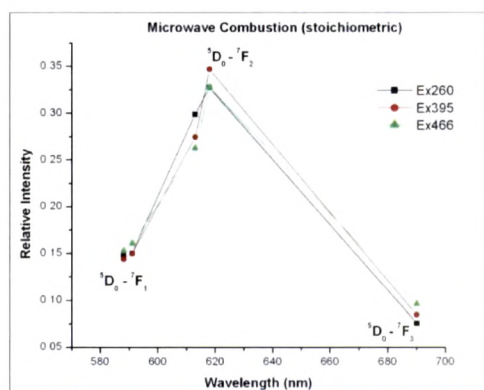
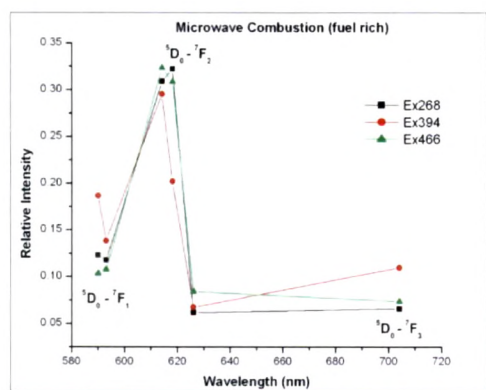
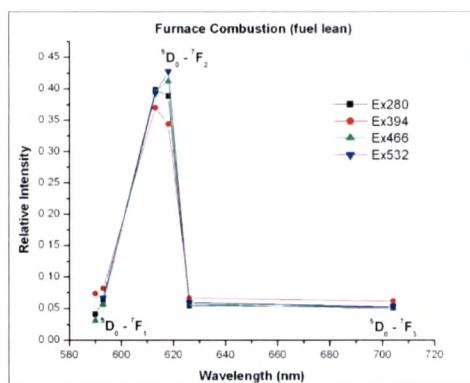
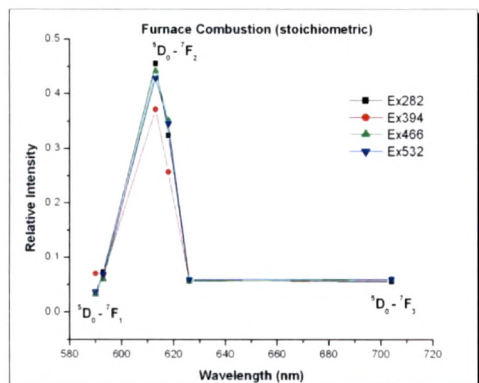
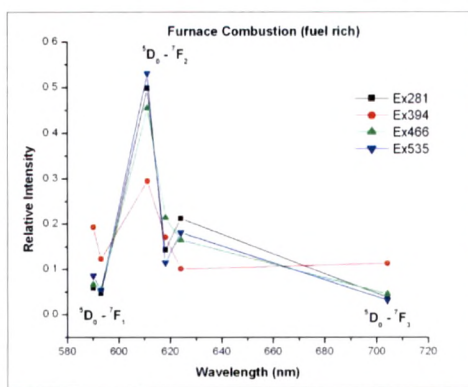
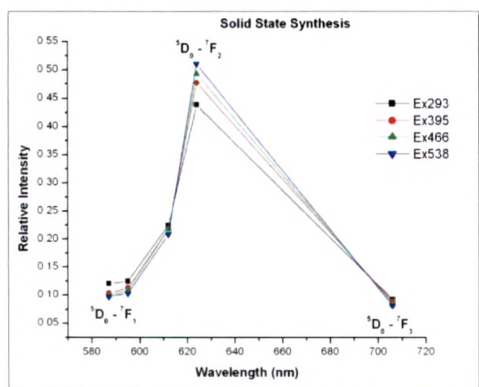
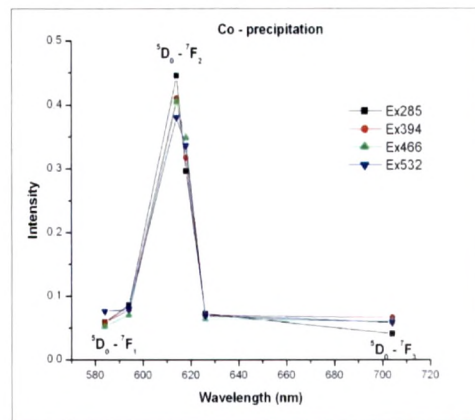
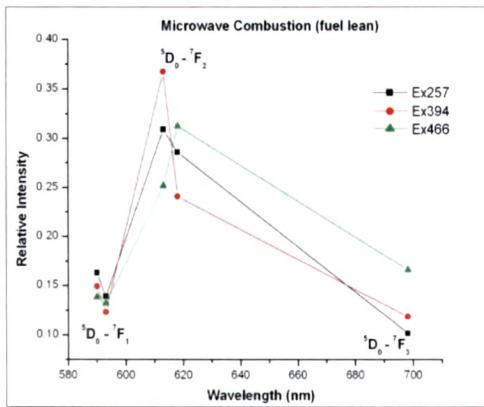


Figure: LEF8b

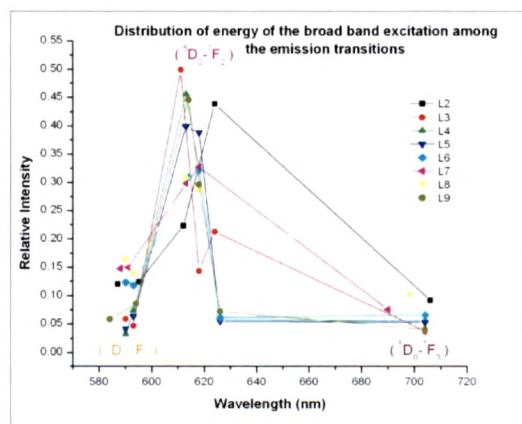
The activation of Lanthanum Oxide by Europium has been reported recently <sup>[35, 36]</sup>. The optical properties of Europium doped Lanthanum Oxide synthesized by different methods have been investigated. For the purpose of reference, one sample has been prepared by the usual method of solid state synthesis. While this method gives bulk material, the combustion methods yield nano crystalline material. For the sake of comparison, one sample was made by co-precipitation method to get nano particles. Thus a range of materials from bulk to nanocrystal to nanoparticles have been synthesized. This is borne out by the XRD results. The fluctuations in the XRD results have been reflected in the fluorescence spectra too.

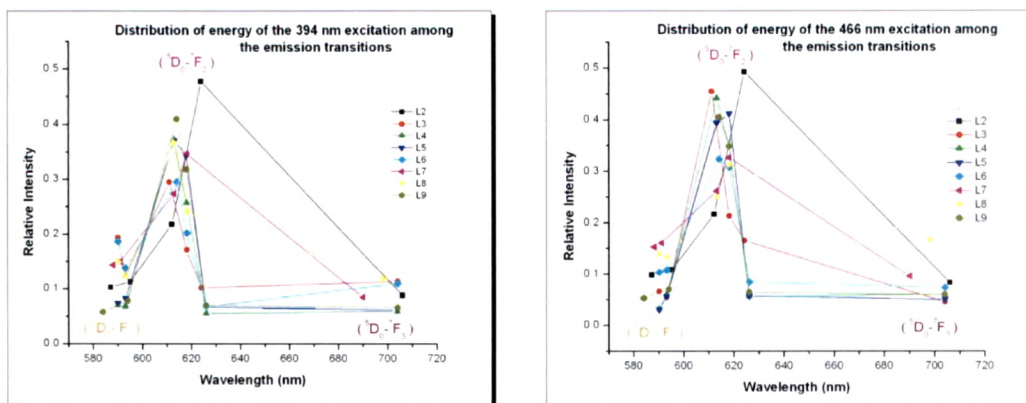
The results of the fluorescence spectra confirm the incorporation of Europium in the lattice in +3 state. The transitions of  $\text{Eu}^{3+}$  are given by  ${}^5\text{D}_0 \rightarrow {}^7\text{F}_J$  ( $J = 0, 1, 2, 3, 4$ ) are authentically pronounced in these spectra <sup>[37]</sup>, albeit with some degree of multiplicity, discussed in the due course. The relative intensities of these transitions vary from sample to sample. Unlike the case of Ceria, the emission features here are dominated by the electric dipole transitions. The major emission peak in all the samples has been found to be between 609 to 626 nm, ascribed to the  ${}^5\text{D}_0 \rightarrow {}^7\text{F}_2$  transitions. The  ${}^5\text{D}_0 \rightarrow {}^7\text{F}_1$  transition corresponding to the 590 nm emission, which operates by magnetic dipole interaction is subdued <sup>[38]</sup>. There are other peaks arising out of the  ${}^5\text{D}_0 \rightarrow {}^7\text{F}_3$  electric dipole transitions <sup>[38]</sup>. These transitions are affected by the crystal field. The distribution of energy among the major peaks is graphically represented in the figures below for the respective samples. The figures give intensity distribution of the emission for the different excitation wavelengths mentioned therein.





It can be seen from the above figures that the intensity distribution over the peaks varies a great deal from sample to sample. There is shift in the peak wavelengths also. The variation of intensities for the different excitation wavelengths does not follow any trend. A common feature turns out to be the multiplicity of the peaks. Peaks are found between 584 to 592 nm, 591 to 595 nm, 611 to 614, 624 to 626 nm and at 618, 690, 698 and 704 nm. The distribution of energy among the emission peaks for the different excitation wavelengths is given below.

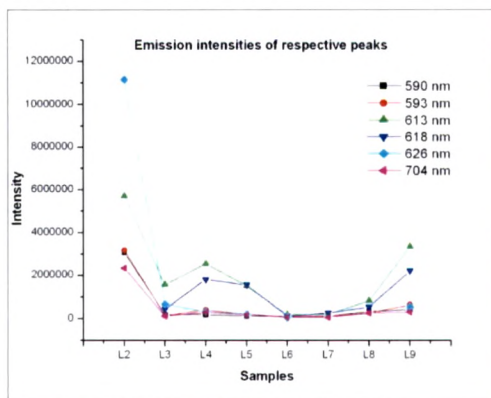




The figure clearly indicates shift in the peak wavelengths and the variation in the distribution of intensities of these peaks for the prepared samples. These shifts and variations are expected, as the samples prepared have different structural parameters. Although these parameters deviate from each other in small proportions from sample to sample, the resultant changes or distortions in the crystal field leads to a variation in the symmetry of the  $\text{Eu}^{3+}$  ions. These changes affect the dipole transitions responsible for energy transfer in  $\text{Eu}^{3+}$  ions. This is the reason for splitting and shifting of the peaks and the variations in intensity.

These results are consistent with other reported emission results <sup>[39]</sup>. It has been noticed that for the broad band excitation of 254 nm,  $\text{Eu}^{3+}$  ions exhibit strong emission at 626 nm. This emission, attributed to the electric dipole transition of  $^5D_0 \rightarrow ^7F_2$  is due to incorporation of  $\text{Eu}^{3+}$  ion at 9-coordination site of the host  $\text{RE}^{3+}$  ion. It is noted that  $\text{Eu}^{3+}$  at 6-coordination, 8-coordination and 12-coordination shows emission at 611, 615 and 626 nm respectively. This information indicates that with increase in coordination of  $\text{Eu}^{3+}$  the emission peak shifts to longer wavelengths <sup>[40]</sup>. In Gadolinium Vanadate with  $\text{Eu}^{3+}$ , the  $^5D_0 \rightarrow ^7F_2$  emission line splits into three components at 609, 615 and 619 nm due to lowering of local site symmetry of  $\text{Eu}^{3+}$  ions. The splitting of various emission lines was also reported in  $\text{Eu}^{3+}$  doped  $\text{MgSiO}_3$  gel and attributed to the lowering of local site symmetry of  $\text{Eu}^{3+}$  ions

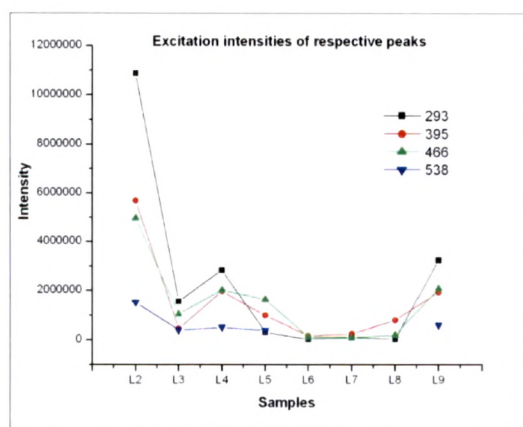
[41]. The intensity pattern of the emission peaks for the prepared samples are given in the figure below.



From the figures given above, it can be seen that the sample made by solid state synthesis (L1) has the highest emission intensity for all the emission peaks. The most intense is the 626 nm peak followed by the peak at 613 nm, which is also intense. There are two peaks at 590 and 593 nm with almost same intensity. It appears like a split in the peak ascribed to the  $^5D_0 \rightarrow ^7F_1$  magnetic dipole transition. There are distinct peaks at 612 nm, 626 nm and 706 nm ascribed to the  $^5D_0 \rightarrow ^7F_2$  and  $^5D_0 \rightarrow ^7F_3$  transitions. Thus, all the standard transitions of  $\text{Eu}^{3+}$  are observed. The 618 nm peak observed in other samples is absent here. Hence, this can be considered as a good reference case.

The sample L9 synthesized by co-precipitation method also shows relatively high intensities of emission peaks, although the distribution changes in comparison to the bulk sample. Here, the 613 nm peak dominates, followed by the 618 nm peak which is nonexistent in the bulk sample. The 626 nm peak is too low in intensity. Hence, there is a complete domination of the electric dipole transitions while the magnetic dipole transitions become almost irrelevant.

Apart from the two samples discussed above, only sample L4 made by furnace combustion method with stoichiometric ratio holds some promise in terms of the intensities of the



emission peaks. The samples prepared by microwave assisted combustion give very poor results.

The variation of intensities of the major excitation peaks for the prepared samples are presented graphically in the figure above. It shows almost the same features as the ones observed in the emission spectra. The absorption is maximum for the sample L2 prepared by solid state method. This is followed by the samples prepared by furnace combustion method (average for L3, L4 and L5) and microwave combustion method (average for L6, L7 and L8). Although the intensities, compared to sample L2, are on the lower side for the sample L9, they are much higher than the samples prepared by combustion synthesis. The sample L9 consists of nanoparticles. With further reduction in particle size and surface passivation, the quantum of the absorbed and emitted energy can be significantly enhanced. This is further supported by the fact that the excitation and emission intensities are almost the same, suggesting nearly cent percent energy conversion of the absorbed energy into the emission lines.

The excitation spectra have a broad band and several narrow band peaks. The spectral positions of the narrow band peaks remain same for all the samples, although the relative intensities vary. However, the broad band shows change in the spectral positions as well as their intensities. The broad band has the maximum intensity in samples L2, L3, L4 and L9.

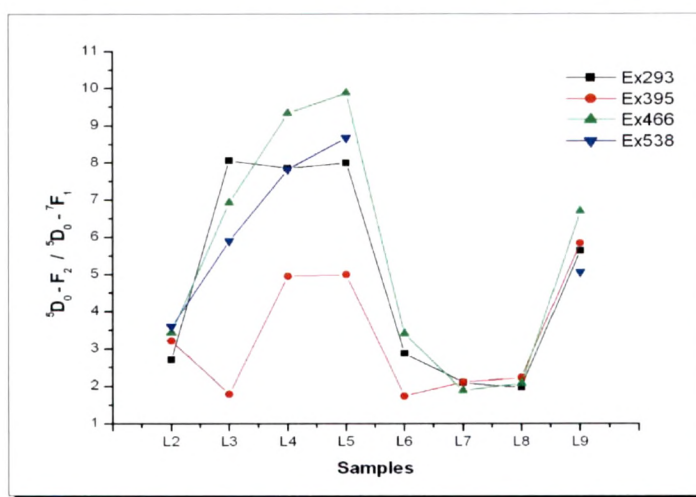
The bulk sample ( L2 ) peaks at 294 nm in this case but a blue shift is observed in the samples L3, L4 and L9, where it peaks around 281 nm. The shift is likely to be a consequence of the lower crystallite size. For samples other than the ones mentioned above, the maximum intensity is seen either for the narrow band peak at 395 nm (samples L6, L7 and L8) or 465 nm (sample L5). In samples L6, L7 and L8, although the broad band intensities are very low, there is a huge blue shift in the peak wavelengths of these peaks. Incidentally, these samples show a higher number of peaks in their XRD pattern also, indicating structural abnormalities.

Looking to the lower wavelengths of these broad band peaks (255nm to 294 nm), the possibility of it being a charge transfer band is very high. Absorption by the host matrix is another possibility, but looks less likely. This view is supported by other studies. The  $O^{2-} - Eu^{3+}$  charge transfer states lie in much higher energy levels, corresponding to a wavelength range of around 274 to 296 nm<sup>[42]</sup>, which is in consonance with the peak values observed in the prepared samples. Besides, the reported values of band gap of Lanthanum oxide is too high<sup>[12]</sup> for appreciable host lattice absorption.

The position of the charge transfer band depends on the  $Eu^{3+} - O$  distance<sup>[43]</sup>. The shorter the  $Eu^{3+} - O$  distance, the larger the energy difference between the 4f electrons of  $Eu^{3+}$  and 2p electrons of  $O^{2-}$  is. Thus, the blue shifts can be attributed to the shorter  $Eu^{3+} - O$  distance in the respective samples.

As the prepared samples result into nano crystallites or nano particles, the size effects as well as the position and symmetry of the activator ions in the modified environment becomes significant. Studies involving site selection spectroscopy done elsewhere<sup>[36]</sup> on  $Eu^{3+}$  activated Lanthanum oxide throws light on these aspects.

The emission spectrum done by this technique is similar to bulk materials. Such excitation and emission spectrum can be attributed to the  $\text{Eu}^{3+}$  ions located at the sites close to the center of the nanoparticles. The variation in the relative intensities of the  ${}^5\text{D}_0 \rightarrow {}^7\text{F}_2$  transitions can be attributed to different local environments surrounding  $\text{Eu}^{3+}$  luminescent centers<sup>[36]</sup>.



The ratio of intensity of the peaks assigned to the electric and magnetic dipole transitions i.e.  $\sum ({}^5\text{D}_0 \rightarrow {}^7\text{F}_2) / \sum ({}^5\text{D}_0 \rightarrow {}^7\text{F}_1)$  which quantifies the degree of distortion from the inversion symmetry of the local environment of  $\text{Eu}^{3+}$  ions in the host lattice, has been graphically represented in the above figure. Due to multiplicity of peaks in both these type of transitions, the summation of intensities of peaks corresponding to these transitions were carried out for the calculation of the ratio. The results show better inversion symmetry for the emission peaks formed by the 395 nm excitation peak. The ratio is quite low for all the peaks of sample L1. This shows that in the sample prepared by solid state synthesis, the  $\text{Eu}^{3+}$  ions are well distributed with a high degree of inversion symmetry. The ratio assumes low values for samples prepared by microwave combustion, although the emission intensities associated with them are quite low and the emission for 532 nm excitation is not seen. The ratio is quite high for the samples prepared by furnace combustion, even as the emission intensities associated with them are quite reasonable.

Thus the distortion in host lattice and lack of inversion symmetry of  $\text{Eu}^{3+}$  ions does not affect their performance as luminescence centers. This immunity is found in rare earth ions due to the shielding effect.

### **$\text{La}_2\text{O}_3: \text{Tb}^{3+}$**

The emission and excitation spectra of the Terbium activated Lanthanum oxide is given below in the figures from LTF1 to LTF8.

Figure LTF1b shows emission spectra of sample L2 synthesized by solid state synthesis. The emission spectrum consists of emission peaks for two different excitation wavelengths 233 and 274 nm. There are four major features observed with the peak at 542 nm having the highest intensity followed by peaks at 486, 587 and 620 nm in the order of decreasing intensities. The main peak has a split nature. The intensities of all the emission peaks are highest for excitation wavelength 274 nm.

Figure LTF1a shows excitation spectra of sample L2 monitored for four different emission wavelengths 486, 542, 587 and 620 nm. There is one broad band at 275 nm which has another small band attached to it at 233 nm having less intensity. The intensity of the broad band is highest for emission wavelength 542 nm and the intensity decreases for the 486, 587 and 620 nm in the same order.

Figure LTF2b shows emission spectra of sample L3 synthesized by furnace combustion method with fuel rich ratio. The emission spectrum is for four different excitation wavelengths 257, 341, 351 and 369 nm. The peak at 541 nm has the highest intensity followed by the peaks at 547, 486, 584 and 620 nm in the order of decreasing intensities. The intensities of the emission peaks are highest for excitation wavelength 257 nm. The intensity decreases for the peaks at 369, 351 and 341 nm in that order.

Figure LTF2a shows excitation spectra of sample L3. The excitation spectrum was monitored for four different emission wavelengths 486, 541, 584 and 620 nm. There is one broad band observed at wavelength 257 nm and four other peaks at 319, 341, 351 and 369

nm. The intensity of the broad band is highest for the monitoring line 541 nm and decreases for 486, 584 and 620 nm monitoring line in that order.

Figure LTF3b shows emission spectra of sample L4 synthesized by furnace combustion method with stoichiometric ratio. It consists of emission lines for two excitation wavelengths 232 and 275 nm. The peak at 542 nm has the highest intensity followed by peaks at 548, 486, 587 and 620 nm in the order of decreasing intensities. The intensities of all the emission peaks are highest for excitation wavelength 275 nm.

Figure LTF3a shows excitation spectra of sample L4 monitored for the respective emission wavelengths 486, 542, 587 and 621 nm. There is one broad band observed at excitation wavelength 275 nm. Attached to it is a small band with peak wavelength 233 nm. The intensities of the broad band are highest for emission wavelength 542 nm and decrease for 486, 587 and 621 nm respectively.

Figure LTF4b shows emission spectra of sample L5 synthesized by furnace combustion method with fuel rich ratio. The emission spectrum is for five different excitation wavelengths 258, 317, 351, 368 and 379 nm. In this case too, the peak at 541 nm has the highest intensity followed by the peaks at 547, 486, 586 and 620 nm in the order of decreasing intensities. There are additional peaks observed at 501 and 603 nm for excitation wavelength 368 nm and a peak at 514 nm for excitation wavelength 378 nm. The intensities of the emission peaks are highest for excitation wavelength 368 nm and decreases for the peaks at 378, 351, 317 and 258 nm in that order.

Figure LTF4a shows excitation spectra of sample L5 monitored for three different emission wavelengths 486, 541 and 587 nm. There is one broad band at 258 nm and multiple peaks at wavelengths 284, 317, 341, 351, 367 and 378 nm. The intensity of the peak at 378 nm is highest followed by intensities of peaks at 367, 351, 341, 317, 284 nm and the broad band at 258 nm in the decreasing order. The intensity of the broad band is highest for the monitoring line 541 nm and becomes very less for the monitoring lines 486 and 587 nm.

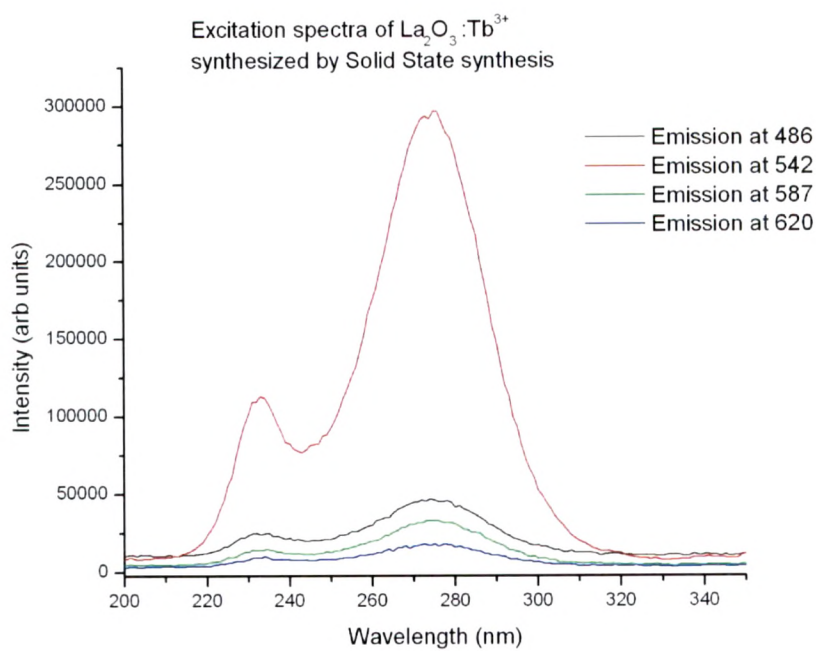


Figure: LTF1a

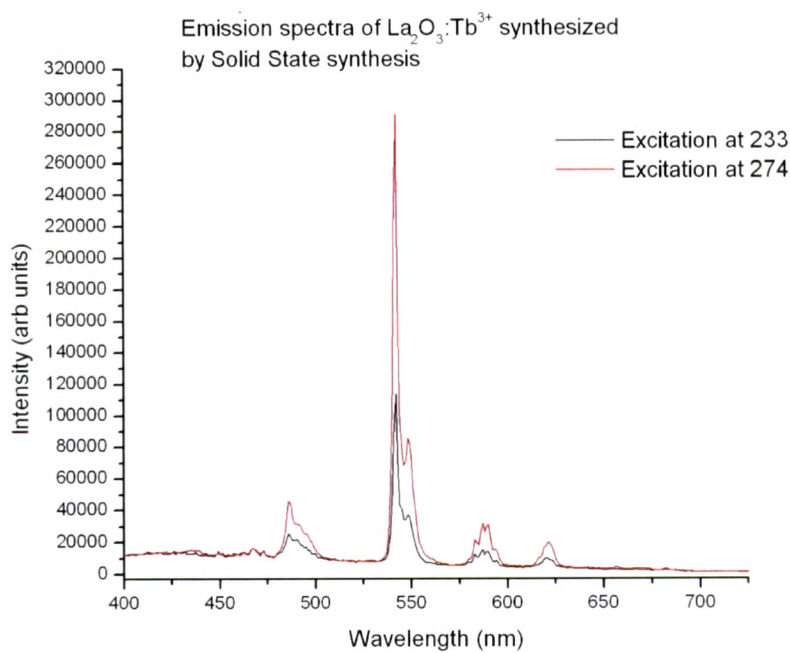


Figure: LTF1b

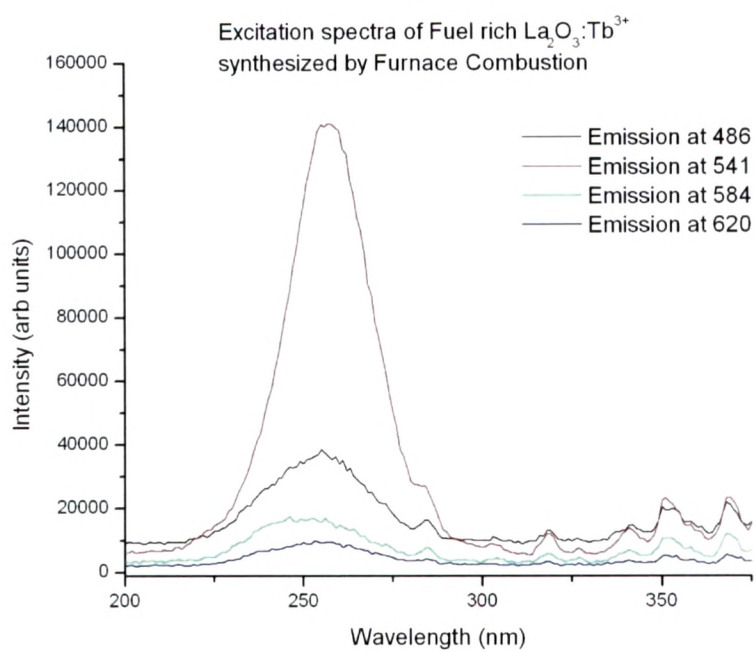


Figure: LTF2a

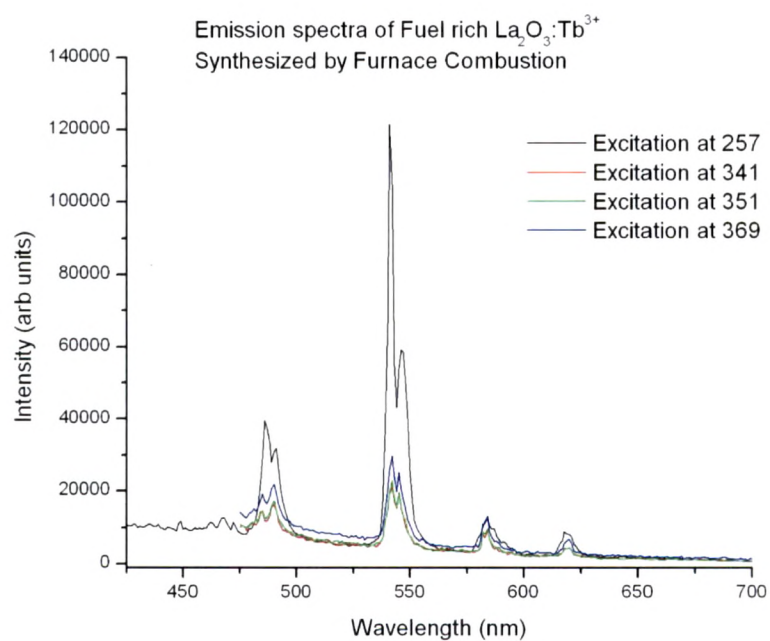


Figure: LTF2b

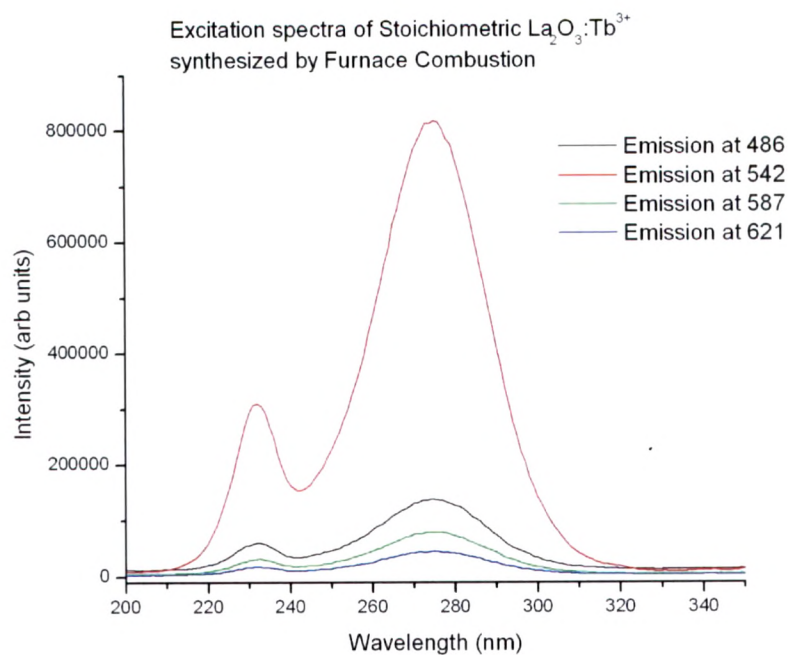


Figure: LTF3a

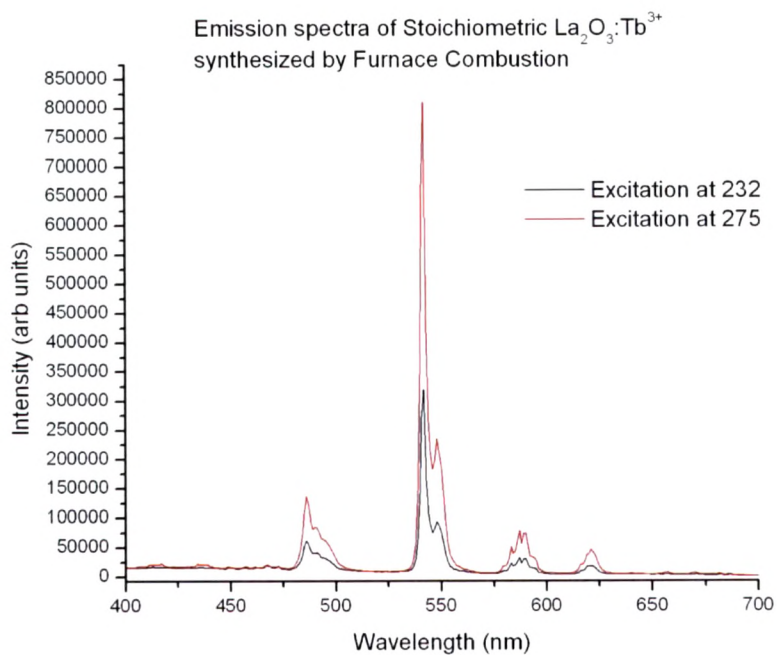


Figure: LTF3b

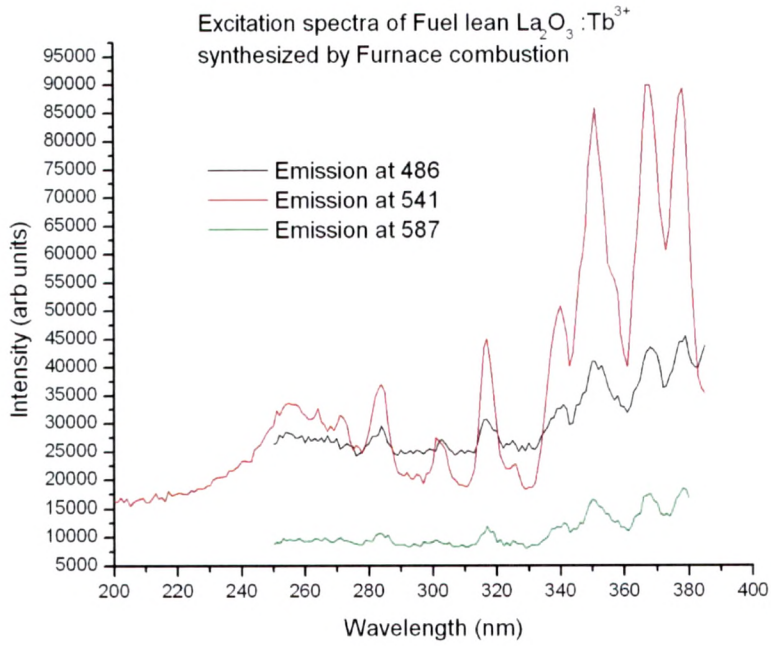


Figure: LTF4a

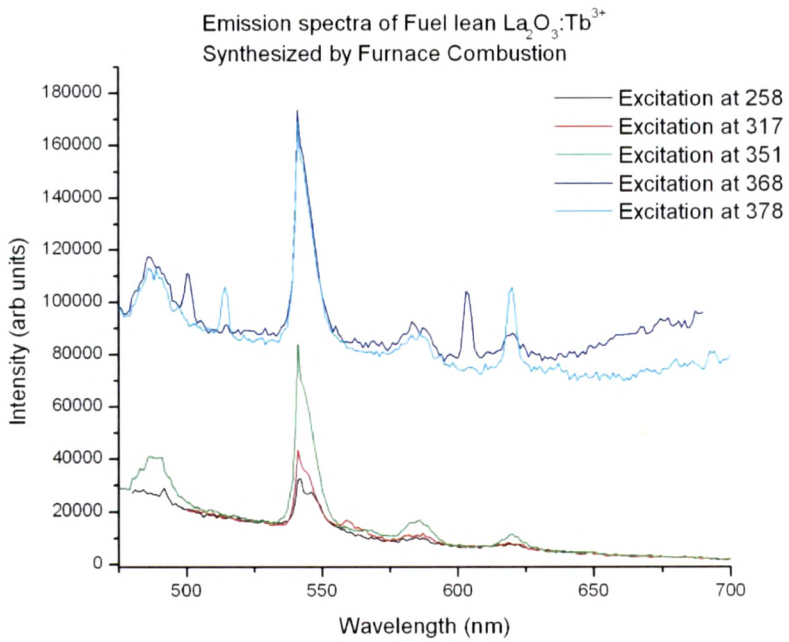


Figure: LTF4b

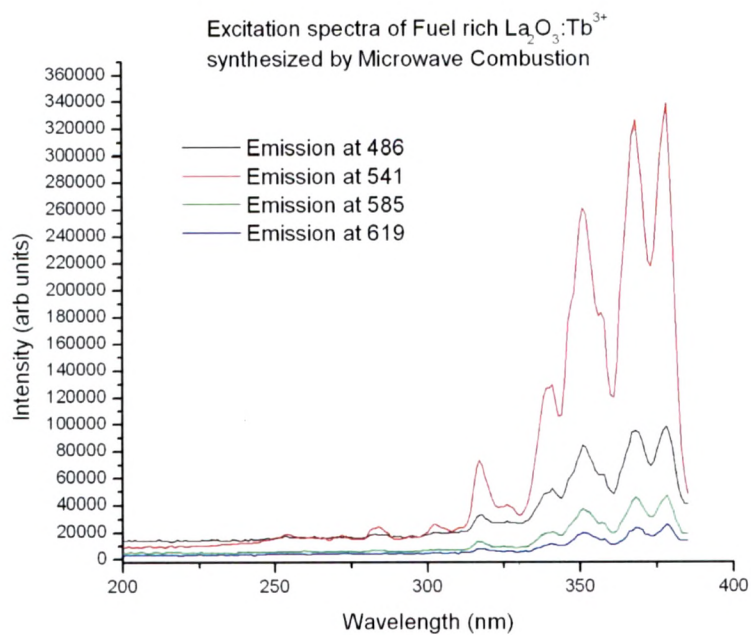


Figure: LTF5a

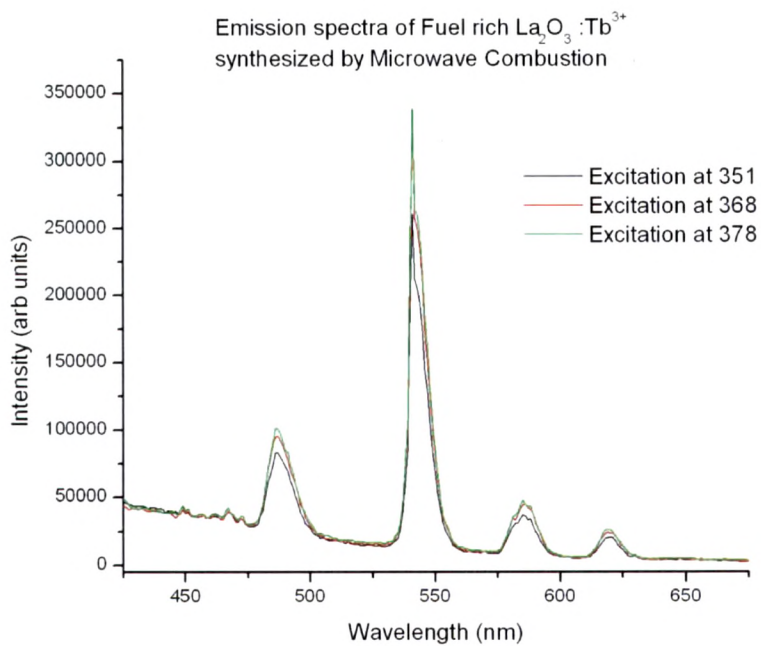


Figure: LTF5b

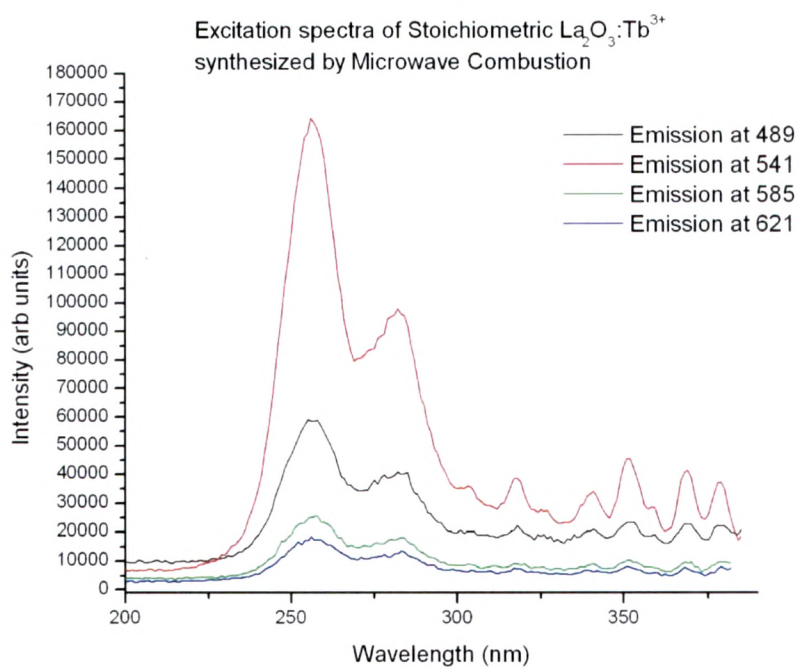


Figure: LTF6a

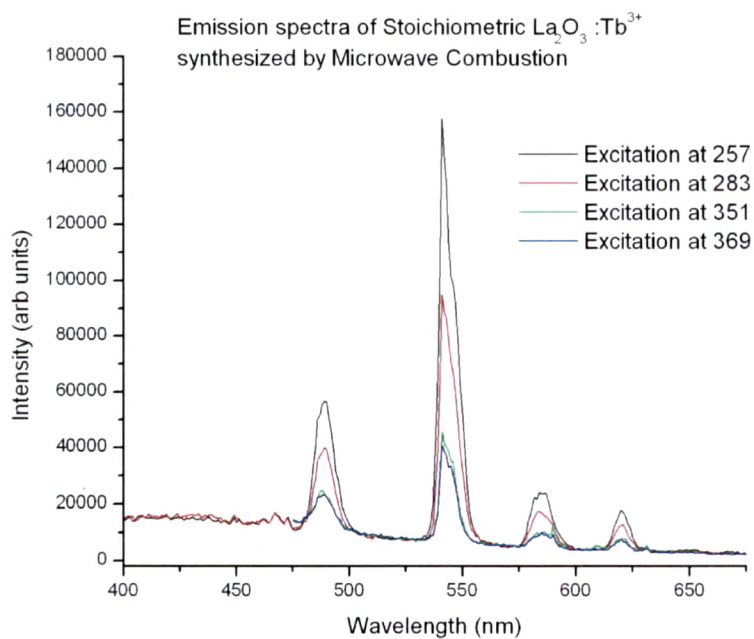


Figure: LTF6b

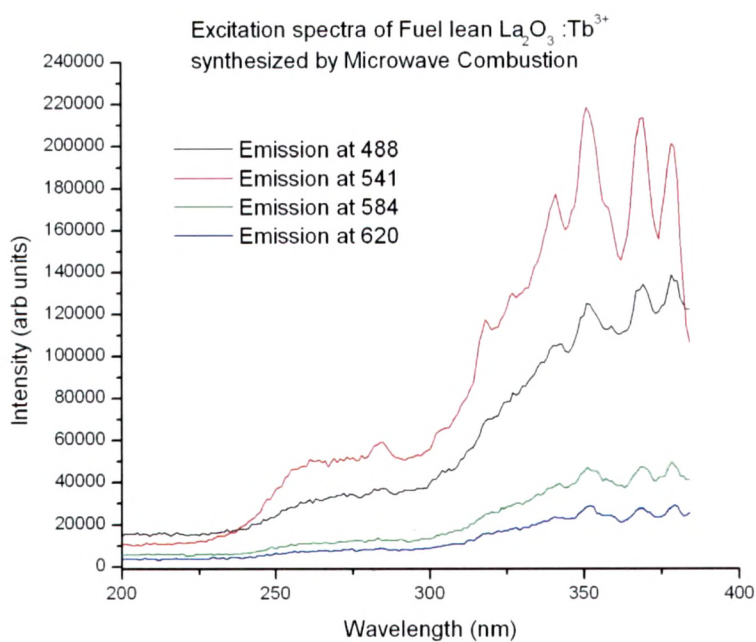


Figure: LTF7a

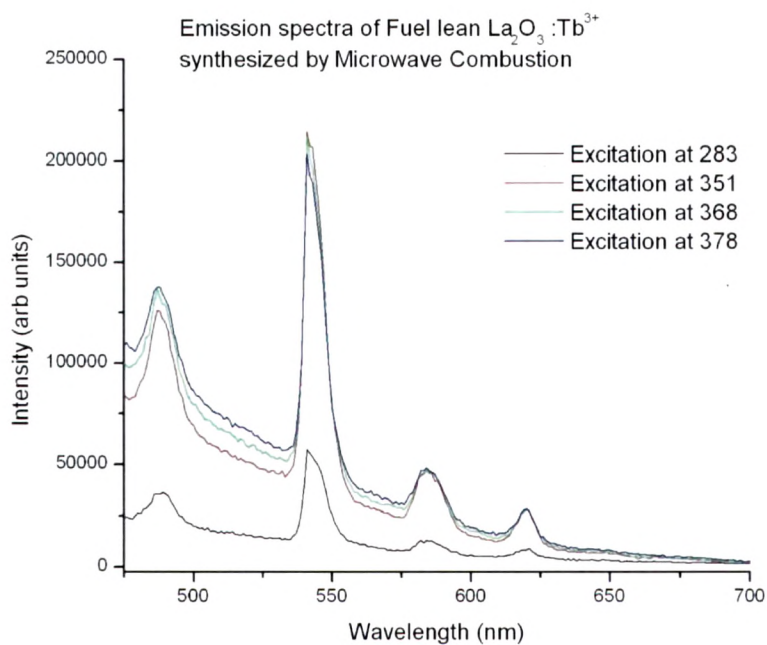


Figure: LTF7b

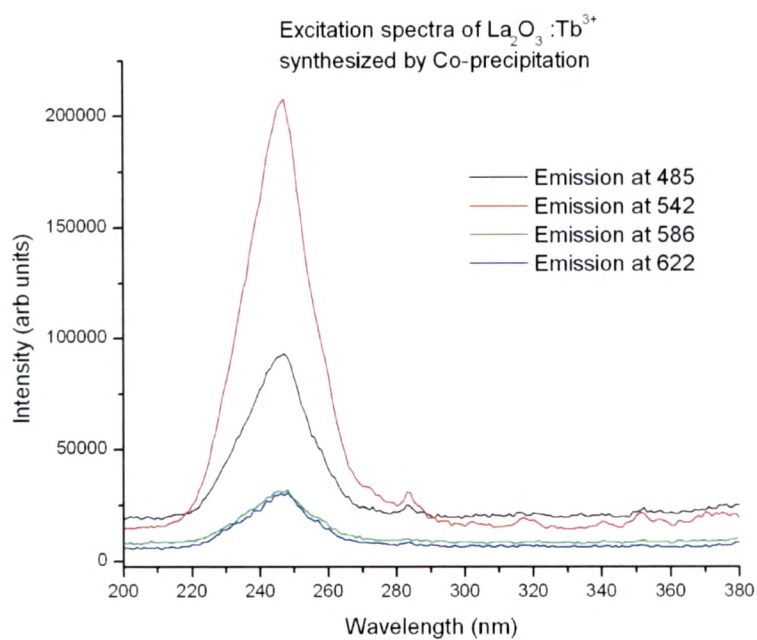


Figure: LTF8a

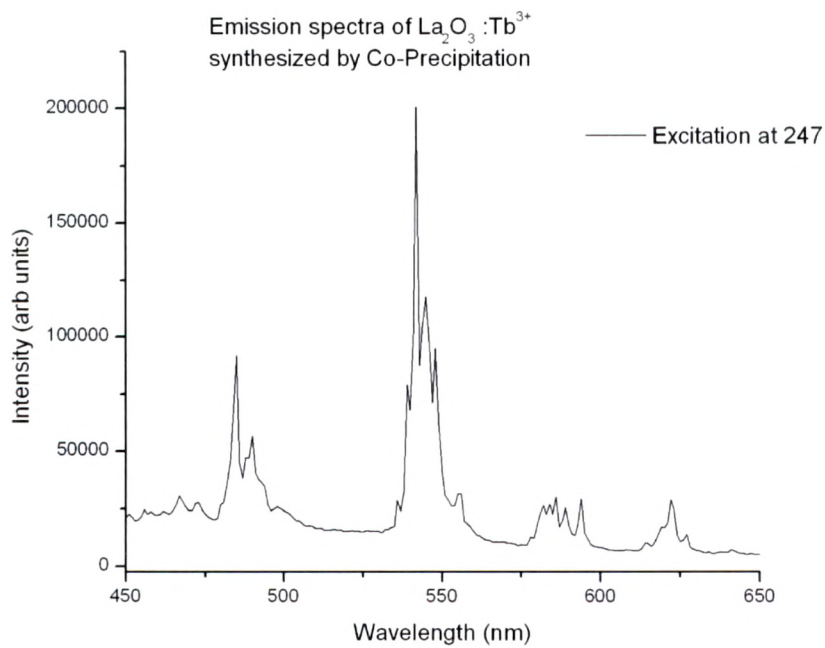


Figure: LTF8b

Figure LTF5b shows emission spectra of sample L6 synthesized by microwave combustion method with fuel rich ratio. The emission peaks are for four different excitation wavelengths 268, 362, 395 and 465 nm. The peak at 614 nm has the highest intensity followed by peaks at 618, 590, 593, 695, 680, 646 and 578 nm in the order of decreasing intensities. In general, the intensities of the emission peaks are highest for excitation wavelength 395 nm followed by excitations at 465, 362 and 268 nm respectively.

Figure LTF5a shows excitation spectra of sample L6 for five different monitoring wavelengths 590, 614, 618 and 695 nm. There is one broad band and several other peaks. The intensity of the peak at 395 is highest followed by peaks at 465, 414, 387, 362 and a broad band at 265 nm in the decreasing order of intensities. In general, the intensity of the excitation peaks is highest for emission wavelength 614 nm followed by those of 618, 590 and 695 nm respectively.

Figure LTF6b shows emission spectra of sample L7 synthesized by microwave combustion method with stoichiometric ratio for four different excitation wavelengths 260, 361, 395 and 465 nm. There are five major peaks with the peak at 617 nm having the highest intensity followed by the peaks at 591, 588, 690 and 646 nm in the order of decreasing intensities. In general, the intensities of the emission peaks are highest for excitation wavelength 395 nm followed with excitation by 465, 260 and 361 nm respectively.

Figure LTF6a shows excitation spectra of sample L7 monitored for three different emission wavelengths namely 590, 616 and 690 nm. The intensity of the peak at 395 nm is highest followed by peak at 465 nm, a broad band at 263 nm and peaks at 375, 361 & 414 nm in the decreasing order of intensities respectively. The intensities of the peaks are highest for emission wavelength 616 nm followed by emission lines 590 and 690 nm respectively.

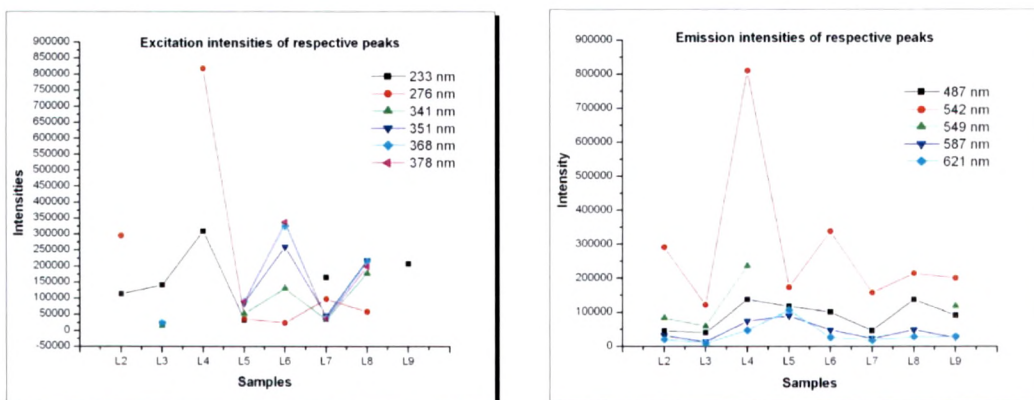
Figure LTF7b shows the emission spectra of sample L8 synthesized by Microwave combustion method with fuel lean ratio for four different excitation wavelengths 257, 361, 394 and 463 nm. There are six noticeable emission peaks with the peak at 612 nm having

the highest intensity followed by the intensities of the emission peaks at 620, 586, 592, 698 and 594 nm in the order of decreasing intensities. In general, the intensities of the emission peaks are highest for excitation wavelength 394 nm followed with excitations by 463, 361 and 257 nm respectively.

Figure LTF7a shows excitation spectra of sample L8 for emission wavelengths 587, 608, 612 and 698 nm. There is one broad band and six other peaks in the spectra. The intensity of the excitation peak at 394 nm is highest followed by intensities of peaks at 464, 382, 375, 361, 318 nm and a broad band at 254 nm in the decreasing order of intensities. In general, the intensities of the peaks are highest for emission wavelength 612 nm followed by the intensities for the monitoring lines 608, 587 and 698 nm respectively.

Figure LTF8b shows emission spectra of sample L9 synthesized by co – precipitation for five different excitation wavelengths 285, 362, 395, 465 and 532 nm. There are eight major and minor peaks observed with the peak at 614 nm having the highest intensity followed by the peaks at 618, 578, 594, 584, 700, 704 and 696 nm in the order of decreasing intensities. The intensities of the emission peaks, in general, are highest for the excitation wavelength 285 nm followed by the excitations of 465, 395, 532 and 362 nm respectively.

Figure LTF8a shows excitation spectra of sample L8 monitored for four different emission wavelengths 578, 594, 614 and 704 nm. There is one broad band and six major peaks. The intensity of the excitation broad band at 285 nm is highest followed by peaks at 465, 395, 395, 532, 362, 380 and 414 nm in the decreasing order of intensities. The intensity of the broad band is highest for emission wavelength 614 nm followed by the intensities of 578, 594 and 704 nm peaks respectively. The variation in the intensities of the excitation and emission peaks of the prepared samples is presented above.



The emission spectra of the samples show peaks corresponding to the usual transitions of  $Tb^{3+}$  ions corresponding to the  ${}^5D_4 \rightarrow {}^7F_j$  ( $j = 4, 5, 6, 7$ ). The 542 nm ( ${}^5D_4 \rightarrow {}^7F_5$ ) emission peak has the highest intensity in all samples. The 549 nm peak is not seen at all in several samples. Some additional peaks, although minor are observed in sample L5. The 542 nm peak in sample L9 shows splitting. There is inhomogeneous broadening in the 590 nm peak [44]. These differences in L9 can be attributed to the surface effects in nano particles.

The consistency in the emission features is not seen in the excitation spectra. The spectra have broad band as well as narrow peaks. It is interesting to note that the samples L2 and L4 have only broad band features. Their excitation spectra consist of one intense broad feature with a small band attached to it. Sample L9 has a single and intense broad band excitation. Samples L6 and L8 do not have a pronounced broad band feature, but their narrow band excitation is on the higher side. In general, the shift in wavelength and intensity of the broad band peaks are substantial.

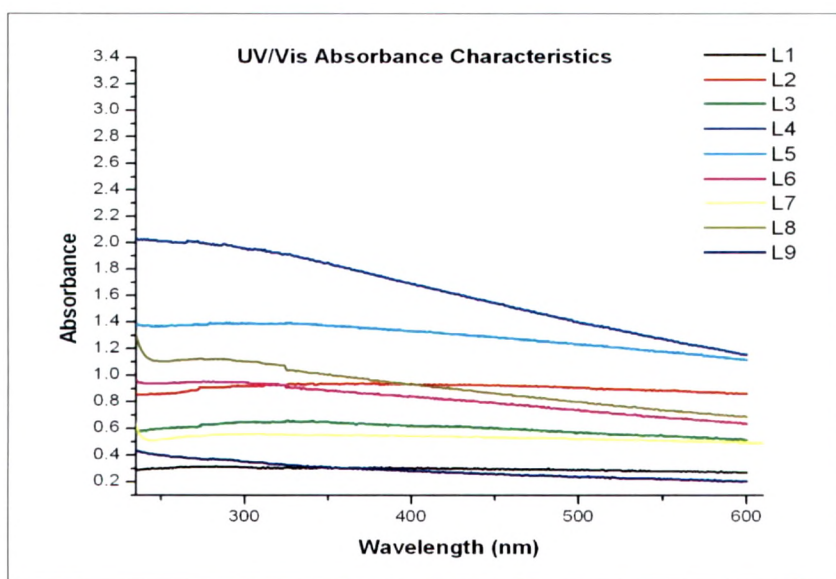
The excitation broad bands are attributed to the  $4f^8 - 4f^75d$  transitions and the longer wavelengths to  $f - f$  transition lines. Upon excitation by the spin-allowed  $4f^8 - 4f^75d$  transition, the emission spectrum can be separated into two groups. There can be blue emission below 480nm from  ${}^5D_3 - {}^7F_j$  transitions and green emission above 480 nm from  ${}^5D_4 -$

${}^7F_J$  ( $J = 4, 5, 6, 7$ ) transitions <sup>[45]</sup>. However, the blue emissions can be observed only for very low concentrations in selected host matrices <sup>[46]</sup>.

The 5d energy level has close relation with the conduction band and therefore the band gap of the compound. The change of 5d energy level is related to factors like the energy centroid of the 5d orbit, crystal field splitting, coulomb interaction between 4f and 5d electrons, spin-orbit interaction of 4f electrons and spin-orbit interaction of 5d electrons <sup>[47]</sup>. The drastic changes in the excitation features of the prepared samples indicate changes in these 5d energy levels on account of the synthesis techniques and synthesis parameters. The presence or absence of the broad band excitation peaks or changes in their relative intensities is in all probabilities, due to the crystal field splitting. This splitting would be in different proportions in different samples, which is borne out by the small differences in the structural parameters as well as the multiplicity of emission and excitation features in the prepared samples.

### **UV – Visible Characteristics**

The samples taken in equal proportion were dispersed in methanol. Each dispersion was sonicated and then transferred to a quartz cuvette for taking the measurements. The wavelength range was fixed between 230 nm and 600 nm. The results are presented in the figure given below.



The spectral absorption characteristics are almost flat in the recorded range. The small variations in absorbance within this spectral range do not enable the precise positioning of peak wavelengths and the corresponding absorbance maximas. This came as a handicap to equate the peak excitation wavelengths with peak absorbance wavelengths, which could have led to corroboration of some results.

The only exception to this is sample L4, which shows maximum absorbance and a gradual decrease in absorbance values with wavelength. Incidentally, the excitation and emission intensities are also higher relative to the other prepared samples.

## References

- 1 S.L. Jones, D. Kumar, R.K. Singh, P.H. Holloway, *Appl. Phys. Lett.* 71 (1997) 404
- 2 D. Kumar, J. Sankar, K.G. Cho, V. Cracium, R.K. Singh, *Appl. Phys. Lett.* 77 (2000) 2518
- 3 R. Raue, M. Shiiki, H. Matsukiyo, H. Toyama, H.Y. Yamamoto, *J. Appl. Phys.* 75 (1994) 481
- 4 S. Itoh, M. Yokoyama, K.J. Morimoto, *J. Vac. Sci. Technol. A* 5 (1987) 3430
- 5 Cao. J, Ji.H, Liu. J, Zheng. M, Chang. X, Ma. X, Zhang. A, Xu. Q, *Mat. Lett.* 59 (2005) 408
- 6 Bo Li and Horia Metiu, *J. Phys. Chem. C* XXXX, xxx, 000
- 7 Campbell, K. D.; Zhang, H.; Lunsford, J. H. *J. Phys. Chem.* 1988, 92, 750
- 8 O.V. Manoilova, *J. Phys. Chem. B* 108: 15770
- 9 Kale, S.S., Jadhav, K.R., Patil, P.S., Gujar, T.P., Lokhande, C.D. *Mat. Lett.* 59 (2005) 3007
- 10 Ding. J, Yang. Q, Tang. Z, Xu. J, Su. L, *J. Opt. Soc. Am. B* (2007), 24, 681
- 11 Chen. H, Liu Y. H, Zhou Y. F., Zhang, Q. Y., Jiang Z. H., *J. Non-Cryst. Solids* 2005, 351, 3060
- 12 Wells, A.F. (1984). *Structural Inorganic Chemistry*. Oxford: Clarendon Press. p. 546
- 13 Wyckoff, R. W.G. (1963). *Crystal Structures: Inorganic Compounds*. New York: Interscience Publishers
- 14 Diane K. Williams, Bipin Bihari, and Brian M. Tissue, *J. Phys. Chem. B* 1998, 102, 916-920
- 15 B. S. Chakrabarty, K. V. R. Murthy, T. R. Joshi, *Turk J. Phy.* 26 (2002), 193-7
- 16 Jan W. Stouwdam, Mati Raudsepp and Frank C. J. M. van Veggel, *Langmuir* 2005, 21, 7003-7008
- 17 F. Rosenberger, *Z. Phys.* 167(349) (1962) 360
- 18 R. C. Ropp, *J. Electrochem. Soc.* 111 (1964) 311

- 19 M. Méndez, J. J. Carvajal, Y. Cesteros, L. F. Marsal, E. Martínez-Ferrero, P. Salagre, P. Formentín, J. Pallarès, M. Aguilò, F. Díaz, *Photonics for Solar Energy Systems III*, SPIE Proceedings Vol. 7725
- 20 H. Song, L. Yu, S. Lu, T. Wang, Z. Liu and L. Yang, *Appl. Phys. Lett.*, 2004, 85, 470
- 21 L. Yu, H. Song, S. Lu, Z. Liu, L. Yang and X. Kong, *J. Phys. Chem. B*, 2004, 108, 16697
- 22 P. Dorenbos, *J. of Lum.* 111 (2005) 89–104
- 23 T.N. Vetchinkina, A.I. Ezhov and Yu.A. Lainer, *Russian J. Inorg. Chem.* 31 (1986) 166
- 24 C. Hodgson, U.S. Patent 2,456,273
- 25 Lauren E Shea, John McKittrick and Olivia A Lopez, *Journal of American Ceramic Society* 79,1996 3257-65
- 26 L A Chick, G D Maupin, L R Pederson, *Nanostructured Materials Vol. 4 No 5*, 1994, Pg 603-615
- 27 C. F. Bacalski, M. A. Cherry, G. A. Hirata, J. M. McKittrick, J. Maurant, *Journal of the SID supplement-1*,2000
- 28 L.A. Chick, L.R. Pederson, G.D. Maupin, J.L. Bates, L.E. Thomas and G. J. Exarhos, *Materials Letters Vol 10*, 1990 pg.6-12
- 29 L.R. Pederson, G.D. Maupin, W.J. Weber, D.J. McReady and R.W. Stephens, *Mat. Lett. Vol 10*, 1991 pg.437- 443
- 30 *X Ray Diffraction - a practical approach*, C. Surnarayana, Grant Norton, Plenum press New York, 1998
- 31 Sutton W H, *Material Ceramic Bulletin*, Vol. 68, Nos. 2,1989, pg.376-386
- 32 N Arul Dhas, K C Patil,*Journal of Solid State Chemistry* 102,1993, pg 440-445
- 33 P. RAVINDRANATHAN, G. V. MAHESH, AND K. C. PATIL, *Journal of Solid State Chemistry* 66,1987, pg 20-25
- 34 M Kitiwan, D Aton, *JSME international Journal Series A Vol. 49 No. 1*, 2006
- 35 S.T. Aruna and K.C. Patil, *NanoStructured Materials Vol. 10. No. 6. pp. 955-964*.1998

- 36 A Vadivel Murugan, Annamraju Kasi Viswanath, Bhalchandra A Kakade, V Ravi and V Saaminathan, *J. Phys. D: Appl. Phys.* **39** (2006) 3974–3977
- 37 Jianjun Chang, Sha Xiong, Hongshang Peng, Lingdong Sun, Shaozhe Lu, Fangtian You, Shihua Huang, *J. of Lum.* **122–123** (2007) 844–846
- 38 Lixin Yu, Hongwei Song, Zhongxin Liu, Linmei Yang and Shaozhe Lu, *Phys. Chem. Chem. Phys.*, **2006**, **8**, 303–308
- 39 J. K. Park, S. M. Park, C. H. Kim, H. D. Park, S. Y. Choi, *J. of Mat. Sci. Lett.* **20**, 2001, 2231 – 2232
- 40 Shaolong Tie, Qiang Su, and Yaqin Qu, *phys. stat. sol. (a)* **147**, 267 (1995); *J. Alloy Comp.* **227**, 1 (1995)
- 41 S. Ekambaram, K.C. Patil, Unpublished paper
- 42 X. Fan, M. Yi, Yu Wang, and Q. Wu, *J. Phys. Chem. Solids* **57**, 1259 (1996)
- 43 J. Ho"lsa" and E. Kestila", *J. Chem. Soc., Faraday Trans.* **91**, 1503 -1995
- 44 H. Hoefdraad, M. Steglman and G. Blasse, *Chem. Phys. Lett.*, **1975**, **32**, 216
- 45 G. Blasse, B. C. Grabmeier, *Luminescent Muter-ids*, Springer-Verlag, Berlin, Heidelberg, 1998
- 46 Jianguo Zhou, Fengying Zhao, Xin Wang, Zhenquan Li, Yan Zhang, Lin Yang, *J. of Lum.* (In press)
- 47 Shigeo Shionoya and William Yen, *Phosphor Handbook*, CRC press, London, 1999
- 48 Shihong Zhou, Zuoling Fu, Jingjun Zhang, Siyuan Zhang, *J. of Lum.* (in press)